Geophysical Journal International

Geophys. J. Int. (2016) **204,** 1–20 doi: 10.1093/gji/ggv416

GJI Marine geosciences and applied geophysics

Seismic velocities within the sedimentary succession of the Canada Basin and southern Alpha-Mendeleev Ridge, Arctic Ocean: evidence for accelerated porosity reduction?

John Shimeld,[1] Qingmou Li,[1] Deping Chian,[2] Nina Lebedeva-Ivanova,[3,*] Ruth Jackson,[1] David Mosher[1] and Deborah Hutchinson[4]

[1] *Natural Resources Canada, Geological Survey of Canada, Bedford Institute of Oceanography,* 1 *Challenger Dr., Dartmouth, Nova Scotia, Canada, B2Y* 4*A2. E-mail: John.Shimeld@nrcan.gc.ca*

[2] *Chian Consulting Incorporated, Dartmouth, Nova Scotia, Canada, B2V* 1*C5*

[3] *Woods Hole Oceanographic Institution, MS* 22*, Woods Hole, MA* 02543*, USA*

[4] *United States Geological Survey, Woods Hole Science Center,* 384 *Woods Hole Rd., Woods Hole, MA* 02543*, USA*

Accepted 2015 September 28. Received 2015 September 15; in original form 2014 December 10

SUMMARY

The Canada Basin and the southern Alpha-Mendeleev ridge complex underlie a significant proportion of the Arctic Ocean, but the geology of this undrilled and mostly ice-covered frontier is poorly known. New information is encoded in seismic wide-angle reflections and refractions recorded with expendable sonobuoys between 2007 and 2011. Velocity–depth samples within the sedimentary succession are extracted from published analyses for 142 of these records obtained at irregularly spaced stations across an area of 1.9E + 06 km^2. The samples are modelled at regional, subregional and station-specific scales using an exponential function of inverse velocity versus depth with regionally representative parameters determined through numerical regression. With this approach, smooth, non-oscillatory velocity–depth profiles can be generated for any desired location in the study area, even where the measurement density is low. Practical application is demonstrated with a map of sedimentary thickness, derived from seismic reflection horizons interpreted in the time domain and depth converted using the velocity–depth profiles for each seismic trace. A thickness of 12–13 km is present beneath both the upper Mackenzie fan and the middle slope off of Alaska, but the sedimentary prism thins more gradually outboard of the latter region. Mapping of the observed-to-predicted velocities reveals coherent geospatial trends associated with five subregions: the Mackenzie fan; the continental slopes beyond the Mackenzie fan; the abyssal plain; the southwestern Canada Basin; and, the Alpha-Mendeleev magnetic domain. Comparison of the subregional velocity–depth models with published borehole data, and interpretation of the station-specific best-fitting model parameters, suggests that sandstone is not a predominant lithology in any of the five subregions. However, the bulk sand-to-shale ratio likely increases towards the Mackenzie fan, and the model for this subregion compares favourably with borehole data for Miocene turbidites in the eastern Gulf of Mexico. The station-specific results also indicate that Quaternary sediments coarsen towards the Beaufort-Mackenzie and Banks Island margins in a manner that is consistent with the variable history of Laurentide Ice Sheet advance documented for these margins. Lithological factors do not fully account for the elevated velocity–depth trends that are associated with the southwestern Canada Basin and the Alpha-Mendeleev magnetic domain. Accelerated porosity reduction due to elevated palaeo-heat flow is inferred for these regions, which may be related to the underlying crustal types or possibly volcanic

*Now at: Centre for Earth Evolution and Dynamics, University of Oslo, P.O. Box 1048, Blindern 0316, Oslo, Norway.

intrusion of the sedimentary succession. Beyond exploring the variation of an important physical property in the Arctic Ocean basin, this study provides comparative reference for global studies of seismic velocity, burial history, sedimentary compaction, seismic inversion and overpressure prediction, particularly in mudrock-dominated successions.

Key words: Numerical approximations and analysis; Spatial analysis; Controlled source seismology; Acoustic properties; Sedimentary basin processes; Large igneous provinces; Crustal structure; Arctic region.

1 INTRODUCTION

The borderlands of the Canada Basin beneath the Arctic Ocean comprise the continental terrace of North America to the south and east, the Northwind and Mendeleev ridges to the west, and the Alpha Ridge to the north (Fig. 1). Geological exploration of this remote marine region generally involves expensive operations such as icebreakers or aircraft-supported camps on the perennial sea ice. As a result, properties of the sedimentary succession and the underlying crust were essentially unknown until the 1960s (Ostenso 1962). Most of the sedimentary basin lies beneath an abyssal plain area of about 0.5 million km^2, where the water depth ranges between 3.5 and 3.9 km. Its northern and western reaches include the Nautilus and Stefansson basins, which are two physiographic provinces defined by Jakobsson *et al*. (2003). Geological sampling is sparse. Dredges and piston cores provide information on seafloor sediments and possible subcropping units at widely spaced sites (e.g. Mudie & Blasco 1985). The only scientific boreholes, drilled in 2004 during Expedition 302 of the Integrated Ocean Drilling Program, are located on the Lomonosov Ridge more than 1000 km to the north of central Canada Basin (Moran *et al*. 2006). Over 500 industry wells have been drilled along the Arctic Alaska and Beaufort-Mackenzie margins (Spencer *et al*. 2011), but these penetrate mainly nearshore successions that are unlikely to be present in the deep-water basin.

To increase understanding of the region, the Geological Survey of Canada directed five seismic surveys between 2007 and 2011. The Canadian Coast Guard Ship *Louis S. St-Laurent*, an Arctic Class 4 icebreaker, was used as a seismic platform with conventional source and receiver systems modified for operation beneath the icepack. Under a collaborative agreement with the U.S. Geological Survey, the U.S. Polar Class Coast Guard Cutter *Healy* was operated as a lead icebreaker ahead of the *Louis* during the last four survey years. In total, the five surveys yielded 15 481 km of seismic reflection data (16-channels; maximum source-to-receiver offset of 226 m), 154 wide-angle seismic reflection/refraction records acquired with expendable sonobuoys (maximum source-to-receiver offsets of 40 km), 18 000 km of multibeam bathymetry, and 38 000 km of single beam bathymetry. Details regarding each survey are available in the associated expedition reports (Jackson *et al.* 2008, 2009; Mosher *et al.* 2009, 2011, 2012a), while an overview of the operations is given by Hutchinson *et al*. (2009). Examples illustrating the quality of the seismic data and also showing regional transects of the basin are provided in several recent publications (Mosher *et al*. 2012b,c, 2013). Analyses of the expendable sonobuoy records are provided in a report by Chian & Lebedeva-Ivanova (2015) which includes plots of the raw and processed data, coincident seismic reflection profiles, 2-D velocity layers produced by iterative forward modelling of the data, independent semblance analyses and velocity–time–depth tables.

1.1 Geological synopsis

It is widely speculated that the Canada Basin was created, during opening of the broader Amerasia Basin, by Jurassic–Early Cretaceous rifting and seafloor spreading between the Arctic margins of Alaska and Canada. However, there are numerous models for formation of the basin because the regional tectonic elements and their geodynamic history are poorly known (see Lawver & Scotese 1990 and Miller *et al*. 2010 for overviews and discussion). Uncertainty is particularly high northward where the basin is obscured by the Alpha and Mendeleev ridges, which form an widespread (>1 million km^2), intensely magnetized, submarine magmatic complex extending along an arcuate trend for a distance of 1700 km between the Canadian Arctic and Siberian margins. The Alpha-Mendeleev ridge complex is generally considered to be part of a broader array of onshore–offshore Cretaceous volcanic rocks, dikes, and sills that are collectively referred to as the High Arctic Large Igneous Province (Tarduno 1998; Maher 2001; Drachev & Saunders 2003; Villeneuve & Williamson 2003; Buchan & Ernst 2006). The complex is also associated with the F1 magnetic domain of Saltus *et al*. (2011; indicated on Fig. 13 and all other maps), which they interpret as a distinct geodynamic element of the crust. As reviewed and summarized by Døssing *et al*. (2013), the Alpha-Mendeleev ridge complex is interpreted by various researchers to be: (i) a 30–40-km-thick oceanic plateau or (ii) a volcanic margin, possibly including extended continental blocks or (iii) highly altered, underplated continental material. Geophysical constraints (Sweeney & Weber 1986), and radiometric dating of a single basaltic sample (Jokat *et al*. 2013), suggest that the complex was largely constructed in the Early Cretaceous with late phases of magmatism persisting into the Late Cretaceous. Evidence from shallow core samples indicates that it had subsided and was undergoing burial by the late Campanian or early Maastrictian (Mudie & Blasco 1985; Davies *et al*. 2009).

The continental terrace bounding southern and eastern Canada Basin is composed of a thick (>10 km) sedimentary prism deposited along the rifted margins of Arctic Alaska and Canada (Grantz *et al*. 1990, 2011; Jackson & Oakey 1990; May & Grantz 1990). The prism thins to the north and west with increasing distance from the slope, and it is generally less than 1 km in thickness over the Northwind and Alpha-Mendeleev ridges (Bruvoll *et al*. 2012; Hegewald & Jokat 2013). The sediment provenance is diverse, and it includes the Chukotka magmatic belt, the Brooks Range orogenic belt, the Ellesmerian orogenic belt, the Canadian craton, the Arctic Platform and volcanics associated with the Alpha Ridge (Houseknecht & Bird 2011). Sediment transport into the basin was affected by regional tectonic events that varied through time and with position along the rifted margins, but distinct depocentres formed beneath two areas of the continental terrace (Grantz *et al*. 2011; Houseknecht & Bird 2011; Fig. 11): (1) the shelf and slope of western Arctic Alaska, between about 150

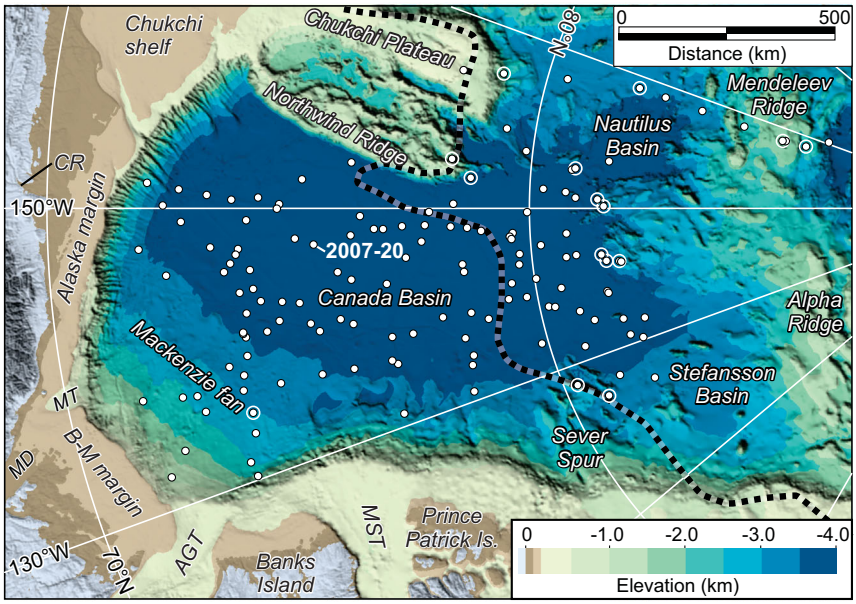

Figure 1. Physiography of the Canada Basin and southern Alpha-Mendeleev Ridge region. Measurements of seismic velocity versus depth within the sedimentary succession were extracted from the results of Chian & Lebedeva-Ivanova (2015) at 142 stations (white dots). Example results from station 2007—20 are shown on Fig. 2. The 15 stations that are circled have less than four velocity–depth pairs. The southern boundary of the Alpha-Mendeleev (F1) magnetic domain (Saltus *et al*. 2011) is indicated by the dashed black line. The bathymetric grid is from version 3.0 of the International Bathymetric Chart of the Arctic Ocean (Jakobsson *et al*. 2012). *AGT*, Amundsen Gulf Trough; *B-M margin*, Beaufort-Mackenzie margin; *CR*, Colville River; *MST*, M'Clure Strait Trough; *MT*, Mackenzie Trough.

and 160°W, which received sediments from the Chukchi shelf and where the succession is estimated to exceed 12 km in thickness; and (2) the Beaufort-Mackenzie shelf where the succession delivered by the ancestral Mackenzie River drainage system may exceed 18 km in thickness. Sedimentation rates in the Alaska depocentre are highest during the early basin history, until the Cretaceous, whereas the rates for the Beaufort-Mackenzie depocentre are highest during the Cenozoic. Significant volumes of sediment were transported into both depocentres, but the overall predominance of the ancestral Mackenzie River is evident from the greater thickness of its depocentre and the wide areal extent of the Mackenzie fan. Laterally extensive, stacked mass transport deposits dominate the upper half of the seismic stratigraphy beneath the slope (Mosher *et al*. 2012b). The abyssal plain is thought to be underlain mostly by unconfined turbidites that are interbedded with amalgamated channel deposits and hemipelagites (Grantz *et al*. 2011). An open marine depositional setting is inferred for the entire post-rift subsidence history.

2 METHODS

Analyses of the sonobuoy records by Chian & Lebedeva-Ivanova (2015) are used in this study to create models of seismic velocity versus depth within the sedimentary succession. The models are valuable for a number of purposes: (i) they provide a statistical characterization of the measured velocities at regional, subregional, and station-specific scales; (ii) they enable 3-D interpolation and extrapolation in a smooth, non-oscillatory, physically plausible manner; (iii) they are well-suited for geological interpretation and comparison with other data sets because the functional form of the models is compatible with established mechanical compaction behaviour and the model parameters can be related to bulk physical properties of the sedimentary succession and (iv) they can be solved for seismic time-depth conversion to a high level of numerical precision. More broadly, the sample range and density of the Chian & Lebedeva-Ivanova (2015) data set are, at least to our knowledge, unprecedented for such an extensive geographic region. Therefore the models should be of interest as comparative reference for global studies of velocity–depth trends, burial history, sedimentary compaction, seismic inversion, and overpressure prediction (Japsen *et al*. 2007). The following sections describe the Chian & Lebedeva-Ivanova (2015) data, the sample set that was extracted for this study, the formulation of the velocity–depth models, and the numerical regression techniques that were used to determine the best-fitting model parameters.

2.1 Seismic velocities from sonobuoy records

Seismic ray-tracing and iterative forward modelling was used by Chian & Lebedeva-Ivanova (2015) to create 2-D velocity models for 142 of the sonobuoy records from the Canada Basin and southern Alpha-Mendeleev Ridge (data on the remaining records are not suitable for the analysis). Data pre-processing steps included a correction for delay in firing of the airguns, and also for attenuation of the seismic energy with offset. The record lengths were doubled by merging adjacent traces, which improved the accuracy of the calculated source-to-receiver offsets by enabling identification of direct arrivals through the water column at offsets of up to 30 km. The records were then geometrically aligned in distance with the corresponding seismic reflection profile for iterative forward modelling.

Chian & Lebedeva-Ivanova (2015) observed that most sonobuoy records from the region exhibit up to a dozen refracted arrivals from the sedimentary succession. They applied a transformation to the sonobuoy records called reduced normal move-out, which allows a one-to-one visual correlation of wide-angle reflections with events on the adjoining multichannel seismic profile at zero offset. This transformation enables the 2-D velocity structure to be determined through an iterative approach of forward modelling via an

interactive computer display. Benefits of this approach include: (i) visual confirmation that the proper recording geometries and offset corrections have been applied; (ii) the details of various phase patterns can be investigated at wide angles by perturbing the reduction velocity for the sonobuoy and, (iii) numerous refractions from the sedimentary succession can be analysed efficiently to maximize the velocity information obtained from the record.

Initial 2-D velocity layers were created in the time domain through inspection of the reduced normal-moveout sonobuoy record and digitisation of prominent horizons on the adjoining seismic reflection profile. Velocities were assigned to each layer using the measured slopes of the associated refracted arrivals. The layer boundaries were then converted to depth, and seismic ray paths were determined using the algorithms developed by Zelt & Smith (1992) and Zelt & Forsyth (1994). The resulting travel time versus offset curves were compared to the refracted phases recorded at source-to-receiver offsets of typically 8 to 40 km. For additional control, especially in the shallow succession, the travel time curves of wide-angle reflections were also calculated for each forward model layer and compared to the corresponding phases on the transformed sonobuoy record. Then, beginning with the shallowest model layer, the layer boundaries and velocities were adjusted incrementally and seismic raytracing was re-applied to update the model. This process was continued through progressively deeper layers until the calculated refraction and wide-angle reflection curves of every layer matched the recorded phases. An example from central Canada Basin is shown on Fig. 2.

To investigate the sensitivity of their modelling procedure, Chian & Lebedeva-Ivanova (2015) applied random velocity perturbations to 14 of the forward 2-D velocity models selected from all acquisition years and across the entire survey region. With this approach they concluded that uncertainties in the forward-modelled depths and velocities are generally less than 4 per cent. The value approaches 7 per cent in situations for which the refracted phases are not observed and wide-angle reflections are the only constraint. Mainly these situations are for burial depths of less than 1.5 km, and they represent less than 15 per cent of the measurement set.

2.2 Extraction of seismic velocity samples

The Chian & Lebedeva-Ivanova (2015) results comprise 2-D velocity layers from the depth domain seismic ray-tracing model, with discrete velocities assigned to the top and base of each layer. A sample set of velocity–depth pairs was created from these results by calculating the average interval velocity at the middle of each 2-D layer (Fig. 2). The samples were generally extracted at a source-to-receiver offset of 8 km in the ray-tracing model, as this usually corresponds with the highest density of seismic ray coverage. An offset location of 4 km was used for cases in which the sedimentary thickness is less than 2.5 km, and an offset of 0 km was used for rare cases having severe topography (e.g. across the top of seamounts).

Interval velocities were extracted only for sedimentary layers since velocities of the underlying crust are being analysed in several ongoing studies. The base of the sedimentary succession, hereafter called the base horizon, was interpreted using the seismic reflection profile adjoining each sonobuoy record. Across central and northern Canada Basin, as well as southern Alpha Ridge, the base horizon corresponds to a significant positive impedance contrast which is comparable to that observed at the seafloor (Fig. 2). The impedance contrast across southern Canada Basin is reduced by the effects of deep burial and, in some locations, high levels of noise. Nonetheless, even in these locations the base horizon can generally be identified with a high level of confidence through seismic facies interpretation. Indications of layering, onlap, downlap and truncation are observed above the base horizon, while the underlying crystalline basement typically exhibits transparent or chaotic reflection facies. In some instances, a sharp increase in seismic velocity also marks the position of the base horizon. Seismic basement (i.e. the deepest horizon that can be mapped with reasonable continuity) occurs 0–600 ms beneath the base horizon depending on location within the basin.

The complete set of velocity–depth samples (i.e. velocity–depth pairs) is provided in the online digital supplement to this paper. There are 142 stations in total, distributed irregularly across an area of about 1.9E + 06 km^2 (Fig. 1). The number of samples per station ranges between 1 and 13, and the average is 8. The total number of samples is 1056. Their velocity and depth distributions are summarized on Fig. 3. Roughly half of the samples have velocities of less than 2.0 km s^{-1} and burial depths of less than 1.0 km, but there are 105 samples with velocities greater than 3.8 km s^{-1} and burial depths of greater than 5.9 km. The deepest samples, from depths of up to 10.8 km, have sedimentary velocities approaching 4.9 km s^{-1}.

2.3 Numerical regression modelling of the 1-D velocity profiles

2.3.1 Selection of the functional form

A homogenous, brine-saturated, sedimentary unit undergoing normal compaction comprises a useful scenario for modelling purposes. Three boundary conditions apply to this scenario (Japsen *et al*. 2007): (1) seismic velocity at the surface of deposition is greater than or equal to the critical velocity (i.e. the velocity of unconsolidated sediments at critical porosity, which is the transitional limit above which the sediments are essentially in suspension; Mavko *et al*. 2009); (2) seismic velocity increases with depth to a finite value that is less than or equal to the matrix velocity (i.e. the velocity of the rock at zero porosity) and (3) the gradient of seismic velocity diminishes with depth, ultimately approaching zero as porosity approaches zero.

The exponential functional form satisfies the boundary conditions listed above. It also closely approximates well documented porosity-depth behaviour under normal compaction, at least within the upper 2–3 km of the crust where mechanical processes predominate (Athy 1930; Weller 1959; Magara 1978; Fowler & Yang 1998; Bahr *et al*. 2001; Yang 2001; Revil *et al*. 2002). Chemical compaction exerts significant influence at greater depth, initiating at temperatures of 70–100°C, and it might lead to deviations from strictly exponential porosity-depth behaviour (Bjørlykke 1999). Nonetheless, the exponential form serves as a reasonable approximation and it possesses several mathematical properties that are desirable for modelling (Sclater & Christie 1980; Al-Chalabi 1997a; Japsen *et al*. 2007). A wide range of compaction behaviour can be simulated—from essentially linear to strongly curvilinear—and the resultant curves are both non-oscillatory and asymptotic, making them ideal for interpolation and also bounded extrapolation. Since porosity exerts a strong influence on seismic velocity (Wang 2001), the exponential form is a natural choice for model development in this study.

Any of three domains may be used for modelling: time–depth, velocity–time, or velocity–depth. Chian & Lebedeva-Ivanova (2015) converted their measurements between the velocity–time and velocity–depth domains, but this is a simple linear operation. In contrast, conversion to the time-depth domain acts as a

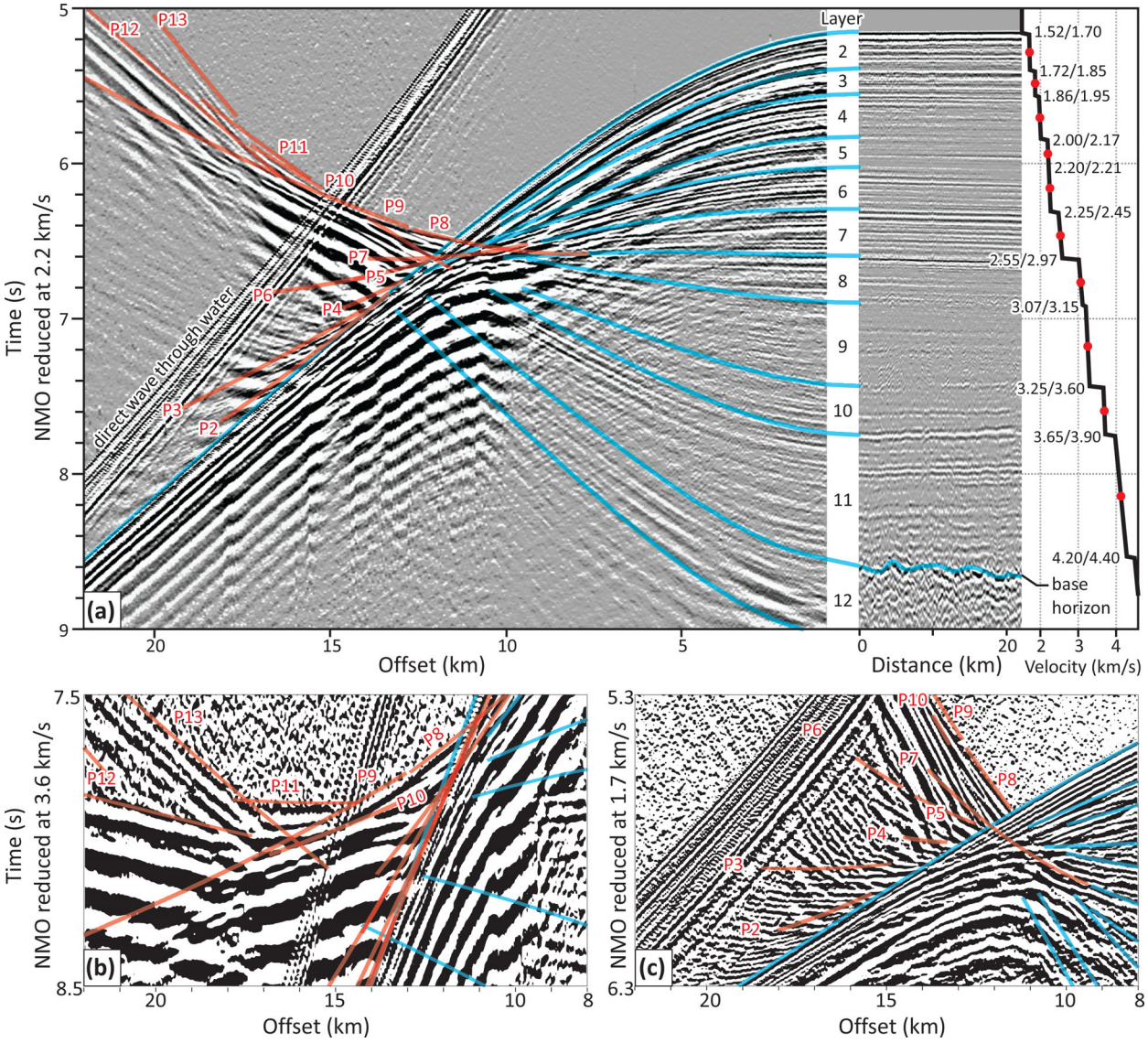

Figure 2. Example 2-D raytrace modelling results from Chian & Lebedeva-Ivanova (2015). a) On the left is the normal moveout corrected record from sonobuoy station 2007–20 (see Fig. 1 for location). The red lines indicate refracted phases, and the blue lines indicate reflected phases. Phases P2 through P12 travelled through the sedimentary succession, while P13 passed through the underlying crust. At zero offset (i.e. the sonobuoy deployment location), the wide-angle reflection phases correspond to the velocity layer boundaries, and these can be traced onto the adjoining seismic reflection profile (LSL0706a) on the right. The velocity–depth profile extracted at a source-to-receiver offset of 8 km is shown in the graph on the extreme right, with velocities at the top and bottom of each layer labelled in km s^{-1}. The red dots indicate the average interval velocities that were used for the present study. (b) and (c) are the same sonobuoy record transformed using different normal-moveout reduction velocities to show the refracted phases in greater detail.

strong smoothing filter (Etris *et al*. 2001) which in some instances might obscure the significance of variance in the measurements. Hence, the velocity–depth domain was chosen for this study since it offers the added benefit of direct comparison with established compaction theory and with published measurements from boreholes.

The following exponential model was proposed by Al-Chalabi (1997a,b):

$$\frac{1}{v\,(h)} = \frac{1}{V_\infty} + \left(\frac{1}{V_0} - \frac{1}{V_\infty}\right) \mathrm{e}^{-\alpha h}, \qquad (1)$$

where $v(h)$ is the velocity as a function of depth below seafloor h. The model parameters V_0, V_∞ and α are well-suited for geological interpretation because they can be related to physical properties. Initial velocity, V_0, represents the velocity of the sediments at the surface of deposition before any significant degree of compaction has occurred (Japsen *et al*. 2007). Final velocity, V_∞, is the asymptotic bound of the sedimentary velocity at infinite depth, which approaches the velocity of the bulk sedimentary matrix as compaction progresses and porosity approaches zero (Japsen *et al*. 2007). Finally, the exponential decay coefficient, α, defines the decreasing rate at which the modelled velocity approaches V_∞ at depth. Broadly speaking, this parameter responds to changes in the elastic moduli of the rocks with increasing burial (Section 4.3.3).

The overriding control on accuracy is the distribution of the samples and the degree to which they conform to the chosen model of velocity–depth behaviour. In circumstances involving complex geology (e.g. a diverse lithological range such as high-velocity carbonates with low-velocity sandstones) it may be necessary to create a multilayer model, possibly even having different functional forms for each layer (Al-Chalabi 1997a). However, in the present sample

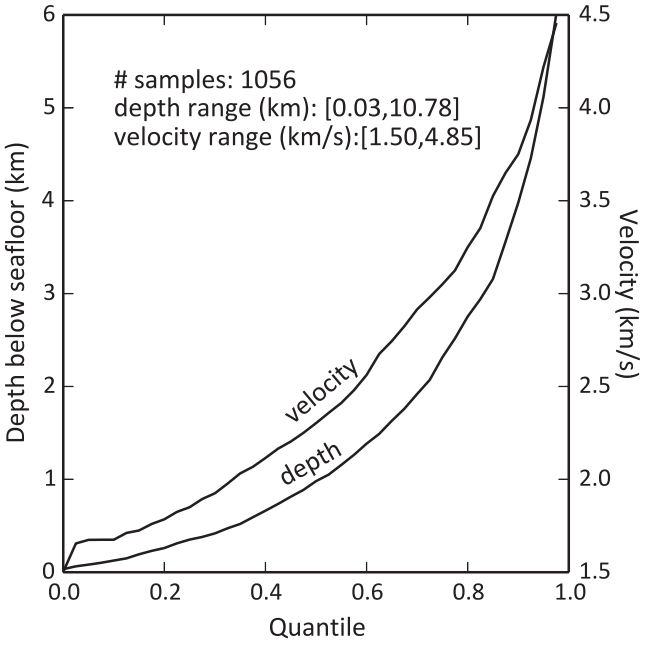

Figure 3. Cumulative sample distributions for the depth-velocity pairs extracted for 142 station locations using the 2-D ray tracing models of Chian & Lebedeva-Ivanova (2015).

set there is no evidence that multiple velocity layers are warranted at either a regional or subregional scale. A single-layer velocity–depth model is adopted, using eq. (1) with parameters that are allowed to vary spatially. This approach ultimately enables the velocity–depth trends of the sample set to be identified and mapped on a station-by-station basis.

2.3.2 *Regression method*

To increase the stability of the regression method, eq. 1 can be rearranged as follows:

$$v'(h) = \ln\left(\frac{V_\infty}{v(h)} - 1\right), \tag{2}$$

where $\beta = \ln(\frac{V_\infty}{V_o} - 1)$. A variable $v'(h)$ is then defined such that:

$$v'(h) = \ln\left(\frac{V_\infty}{v(h)} - 1\right). \tag{3}$$

Substitution of β yields a linear function of h:

$$v'(h) = \beta - \alpha h \tag{4}$$

Eq. (4) can now be used with ordinary least-squares linear regression. However, the conventional approach assumes that h is an independent variable for which the errors are negligible. In reality, there are errors associated with both variables, and the error magnitudes increase with depth. A weighted linear regression method (York 1966; Press *et al*. 1992) was therefore applied, under the assumption that the Chian & Lebedeva-Ivanova (2015) estimate of a 4 per cent uncertainty in the sample magnitude is representative for the standard deviation of the sample errors. The logarithmic transformation of eq. (3) requires that the standard deviations for each sample (σ) be modified according to:

$$\sigma' = \frac{dv'}{dv} \cdot \sigma = \frac{-V_\infty}{\left(\frac{V_\infty}{v} - 1\right) v^2} \cdot \sigma. \tag{5}$$

The best-fitting regression parameters were then determined using the following steps:

(1) Define a sequence of final velocity estimates $\hat{V}_\infty = (V_{\max} + \delta)$, where $V_{\max}$ is the maximum velocity of the sample set and δ ranges from 0.001 to 7.000 km at an increment of 0.001 km.

(2) For each $\hat{V}_\infty$, determine estimates for α and β using eq. (4) with the weighted linear regression method, and calculate the corresponding correlation coefficient between the model and the samples.

(3) From the parameter estimate sequences, select the set of best-fitting parameters that corresponds to the maximum correlation coefficient.

(4) Calculate the best-fitting value for the initial velocity using the relation $V_0 = \frac{V_\infty}{e^\beta + 1}$.

2.3.3 *Time–depth conversion*

Integration of eq. (1) yields the following analytical solution for conversion of a given depth below seafloor, H, to the equivalent two-way seismic travel time, *twt*:

$$twt = \frac{2}{V_\infty}\left(H + \frac{e^\beta - e^{\beta - \alpha H}}{\alpha}\right). \tag{6}$$

For the inverse conversion, from time to depth, it is necessary to find the roots of eq. (6) such that:

$$\alpha H - e^{\beta - \alpha H} + \left(e^\beta - \frac{1}{2} \cdot \alpha \cdot V_\infty \cdot twt\right) = 0. \tag{7}$$

This can be solved in an iterative numerical fashion using Newton's method (Press *et al*. 1992) with the following initial estimate of sediment thickness:

$$H_0 = \frac{V_0 + V_\infty}{2} \cdot \frac{twt}{2}. \tag{8}$$

To test the convergence and numerical precision of this approach, a sequence of *twt* was calculated using eq. (6) for H between 0 and 10 km at 5 m intervals. The *twt* sequence was then converted back to a depth series using Newton's method. After just four iterations, differences between the original and the reconverted depth sequence were within ±1 cm over the entire depth range.

3 RESULTS

Beyond their practical application in seismic time-depth conversion, the velocity–depth models are valuable for 3-D visualization and interpretation of the data. In the following sections, a model is first constructed for the entire sample set so that it can be used as a regional reference curve to identify higher-order trends at subregional scales. From these results, a semi-quantitative measure is used to define five subregions, and separate models are then developed for each subregion. Finally, station-specific models are created by determining V_0 and α from the sample set for each station and assigning V_∞ from the appropriate subregion. Mapping of the station-specific model parameters enables velocity–depth profiles to be generated for any location in the study area. The outlying samples for each station are also mapped in order to explore their potential geological significance.

3.1 Regional velocity–depth model

The velocity–depth model depicted on Fig. 4 is constructed using the complete set of 1056 samples from 142 stations in order to

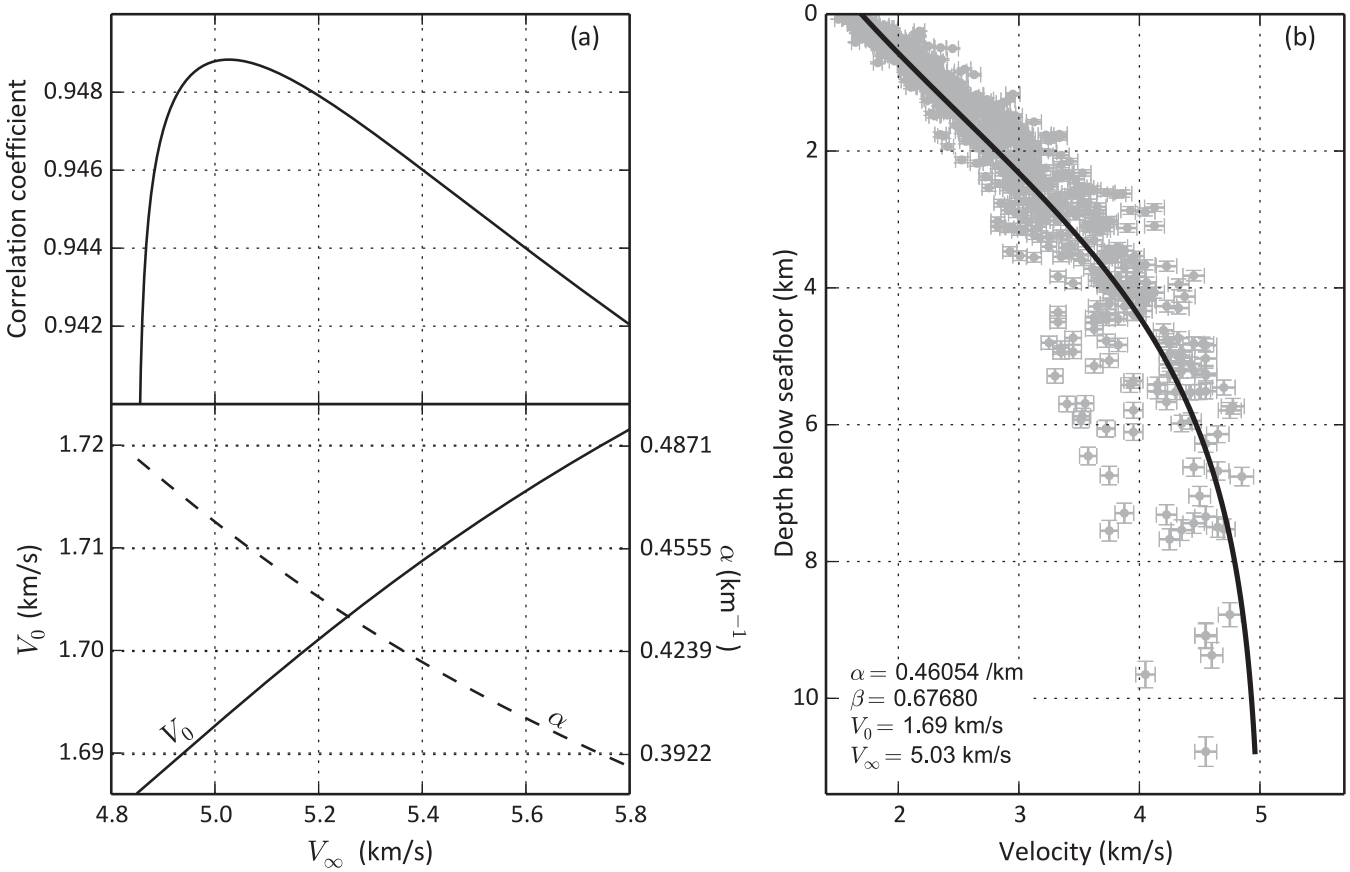

Figure 4. (a) Determination of the best-fitting numerical regression parameters for the regional reference model. The regression estimates for V_0 and α are plotted in conjunction with the correlation coefficient obtained for a range of V_∞. (b) The best-fitting model with respect to the velocity samples. The horizontal and vertical bars indicate the 4 per cent uncertainty ranges from Chian & Lebedeva-Ivanova (2015), which were used as sample weights for the regression.

Table 1. Best-fitting numerical regression parameters for the regional and subregional reference models.

Subregion	α (km^{-1}) std. dev.	β std. dev.	V_0 (km s^{-1})	V_∞ (km s^{-1})
Entire region	0.46054	0.67680	1.69	5.03
	0.00492	0.00570		
1	0.29152	0.66882	1.73	5.09
	0.00979	0.01935		
2	0.32854	0.65105	1.80	5.25
	0.00991	0.01485		
3	0.42745	0.76678	1.69	5.33
	0.00464	0.00652		
4	0.53518	0.77731	1.64	5.20
	0.01090	0.01486		
5	0.63311	0.74126	1.61	4.99
	0.00726	0.00590		

establish a reference for the entire region. The best-fitting numerical regression parameters and their associated standard deviations are listed on Table 1. Geologically plausible values of 1.69 and 5.03 km s^{-1} are obtained for the initial velocity V_0 and the final velocity V_∞, respectively. The value of the exponential decay constant α is 0.46 km^{-1}, and this yields a curvilinear velocity–depth trend that generally matches the observations to within 0.5 km s^{-1}. However, the regional model tends to underestimate velocity at depths above 2 km, and overestimate at depths below 7 km (Fig. 4).

The median of the observed-to-predicted velocity ratios from each station is mapped on Fig. 5. The median values are calculated at 108 stations for which the number of velocity–depth samples is at least five, which ensures that the median statistic is not biased by possible outliers. This criterion corresponds to a minimum sedimentary thickness of about 1.5 km, and thereby excludes areas of the Northwind and Alpha-Mendeleev ridges where the succession is relatively thin and predominantly unlithified (Bruvoll *et al.* 2012; Hegewald & Jokat 2013). The average of the median ratios for the 108 stations is 1.01, confirming that the regional reference model is a reasonably unbiased estimate of the overall sample set, but the 2-D spatial variation of the median ratios is strikingly nonrandom. Low values of the median ratio (<0.97) occur in the southeast beneath the Beaufort-Mackenzie margin, the Mackenzie fan, and the lower slope off Banks Island. High values (>1.03) occur beneath the southwestern Canada Basin, and also northward within the Alpha-Mendeleev magnetic domain. These trends are interpreted to be the result of geological factors since any possible errors in the measurements by Chian & Lebedeva-Ivanova (2015) are unlikely to be so highly systematic. A strong positive correlation ($r = 0.79$) exists between the median ratio and distance from the Beaufort-Mackenzie margin (Fig. 5, inset graph). This correlation hints at a possible association between the median ratio and the total thickness of the sedimentary succession, since the Beaufort-Mackenzie margin is the predominant source of post-Cretaceous sediments in the basin. However, the median ratio exhibits no influence from the thick succession off the Alaska margin. Here, the median ratio clearly increases westward at 90° to the margin (Fig. 5), whereas the sedimentary thickness decreases northward (Fig. 11).

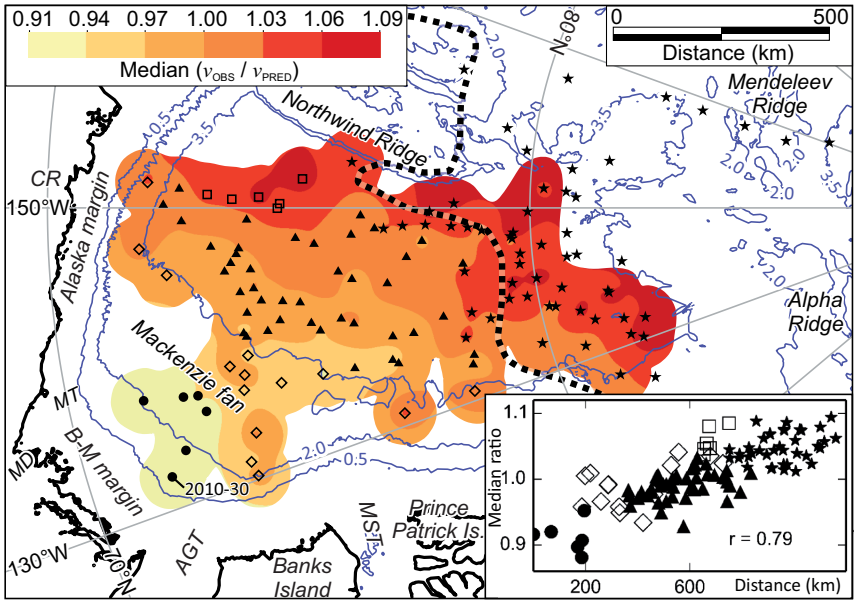

Figure 5. Map of the median observed-to-predicted velocity ratios, calculated using the regional reference model for 108 stations having at least 5 velocity–depth samples. Grid interval: 5 × 5 km. Gridding method: continuous curvature splines (Generic Mapping Tools software package; Smith & Wessel 1990). Inset graph: median ratio versus distance from sonobuoy station 2010–30. Subregions: (1) the Mackenzie fan (circles); (2) slopes beyond the Mackenzie fan (open diamonds); (3) the abyssal plain (triangles); (4) the southwestern Canada Basin (open squares); and (5) the Alpha-Mendeleev magnetic domain (stars). Dashed black line: southern boundary of the Alpha-Mendeleev (F1) magnetic domain (Saltus *et al*. 2011). Solid blue lines: 0.5, 2.0 and 3.5 km isobaths. *AGT*, Amundsen Gulf Trough; *B-M margin*, Beaufort-Mackenzie margin; *CR*, Colville River; *MST*, M'Clure Strait Trough; *MT*, Mackenzie Trough.

To investigate further, each station is assigned to one of the five subregions defined in the following sections, and indicated on Fig. 5. The station assignments are geospatial and therefore involve some interpretation of depositional setting. Nonetheless, the classification is based on straightforward criteria derived from a quantitative measure of the sample distribution about the reference model. More sophisticated numerical classification techniques, such as cluster analysis, are unlikely to add useful information for this phase of the analysis considering that the number of fundamental parameters is small (e.g. spatial location and median ratio). Moderate revisions of the category boundaries have little overall effect on the analysis since the statistical approach is primarily descriptive.

3.1.1 Subregion 1: Mackenzie fan (circles)

The lowest values of the median observed-to-predicted velocity ratio occur at six stations that are located over the upper to middle Mackenzie fan, in water depths of 1.2–2.6 km. For these stations, the average of the median ratios is 0.91, and the standard deviation is 0.024. This distinctive subset of low seismic velocities associated with the fan forms the rationale for subregion 1. A median ratio of 0.95 is used to discriminate between subregions 1 and 2.

3.1.2 Subregion 2: Slopes beyond the Mackenzie fan (open diamonds)

Fifteen stations are located along the continental slopes to the north and west of the Mackenzie fan in water depths of less than 3.5 km. Subregion 2 velocities are typically slower than the reference model, with the average of the median observed-to-predicted ratios being 0.98. The standard deviation, 0.034, is higher than for any other subregion. The maximum median ratio, 1.05, occurs outboard of the M'Clure Strait Trough beneath a bathymetrically complex area of the lower slope.

3.1.3 Subregion 3: Abyssal plain (triangles)

A median ratio criterion of 1.0 ± 0.03 is used for subregion 3, which includes 40 stations across the abyssal plain in water depths of between 3.5 and 3.8 km. Four additional stations, with median ratios of between 0.93 and 0.97, are assigned to subregion 3 simply because they are located in water depths greater than 3.5 km. The average value of the median ratios in subregion 3 is 0.99, and the standard deviation is 0.021, so this sample set corresponds closely with the regional reference model.

3.1.4 Subregion 4: Southwestern Canada Basin (open squares)

The median velocity ratios for six stations in southwestern Canada Basin are distinctly higher than those for nearby stations in subregion 3, and for nearly all other stations at comparable distances from the Beaufort-Mackenzie margin (Fig. 5, inset graph). This phenomenon is unexpected since the gross depositional setting is the same as for subregion 3, so it provides the main rationale for defining a separate subset of the data. The minimum, maximum, average, and standard deviation of the median ratios for subregion 4 are 1.04, 1.08, 1.06 and 0.019, respectively. The average water depth is 3.8 km.

3.1.5 Subregion 5: Alpha-Mendeleev magnetic domain (stars)

Many of the highest median ratio values occur at stations that are more than 750 km from the Beaufort-Mackenzie margin, either within or near the Alpha-Mendeleev magnetic domain (Saltus *et al*. 2011; Fig. 5, inset graph). Stations assigned to subregion 5 exhibit median ratios that, in nearly all cases, are greater than 1.03. This criterion includes nine stations that are located up to 90 km south of the magnetic domain, but which are nonetheless assigned to subregion 5 since the domain boundary itself was derived from geophysical

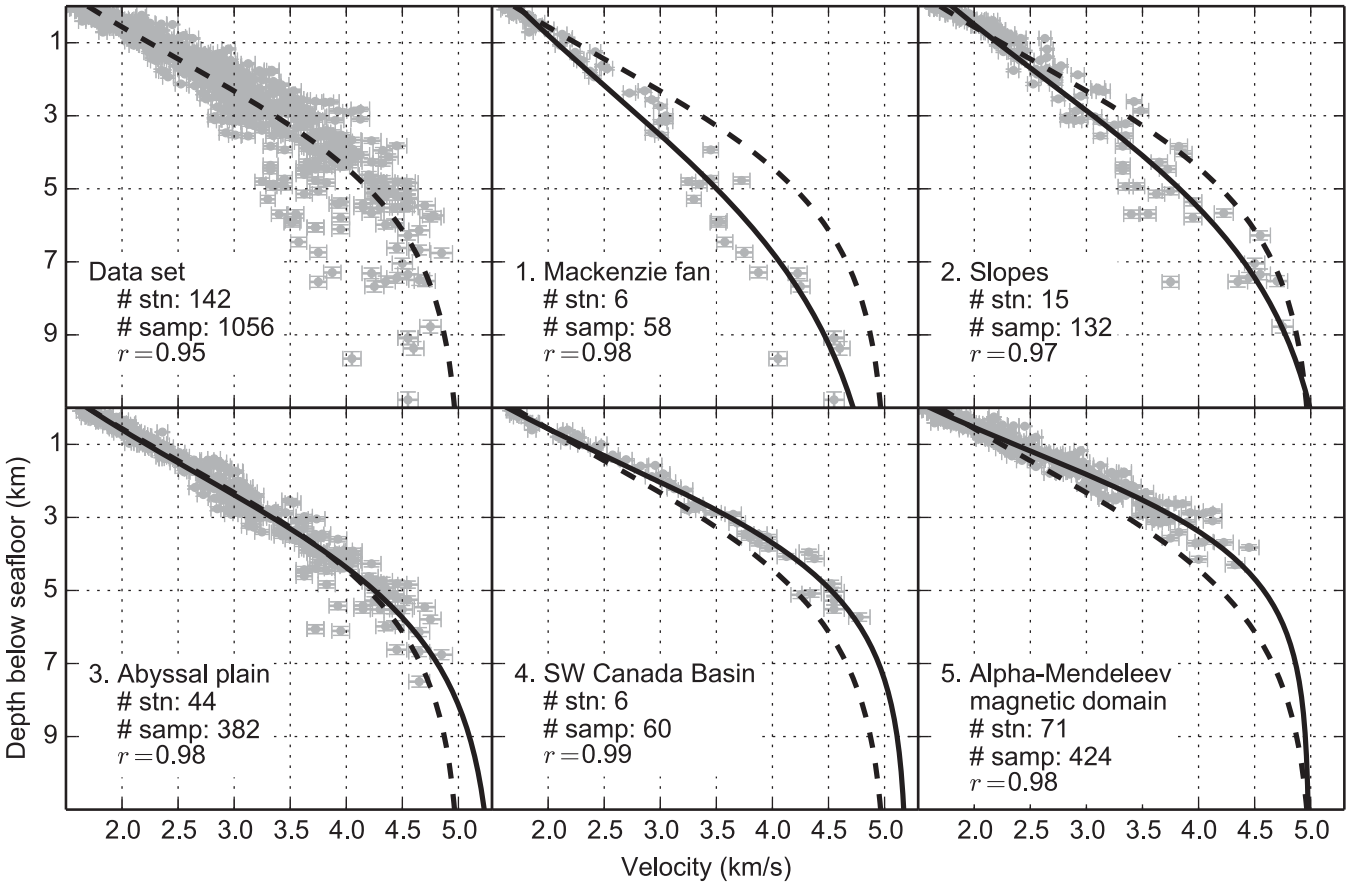

Figure 6. Regional and subregional velocity–depth models for the data subsets that are described in Section 3.1. The regional model (dashed line) is the same as that shown on Fig. 4. Best-fitting parameters for each model are listed in Table 1.

interpretation and may be subject to uncertainty. Seven stations inside the boundary have median ratios of 1.01–1.03, and these are assigned to subregion 5 simply because of their location (and because their velocities are still higher than the regional reference model). Trials in which these stations were assigned to subregion 3 demonstrated little sensitivity in the modelling outcomes. Stations inside the magnetic domain having fewer than five velocity samples (i.e. those for which the median ratio is not calculated) are also assigned to subregion 5. The average, maximum, and standard deviation of the median ratios in subregion 5 are 1.05, 1.09, and 0.023. Water depths range between 0.5 and 3.8 km.

3.2 Subregional velocity–depth models

Plots of the five subregional velocity–depth models are shown on Fig. 6, and the best-fitting regression parameters are listed in Table 1. Each model explains a large proportion of the sample variance within its associated subregion, as is indicated by the correlation coefficients which all exceed 0.97. The sample distributions differ between subregions. In particular, subregion 5 lacks samples from depths greater than 4.3 km. Nonetheless, the predicted V_∞ values are remarkably uniform ($\sigma = 0.12$ km s^{-1}), and are also close to that obtained for the regional reference model (5.03 km s^{-1}). Such consistency demonstrates that the methodology can produce stable estimates for V_∞ even when deep samples are unavailable.

In subregions 1 through 3, a number of the samples from depths of about 5–7 km are slower than their respective models, but these samples do not necessarily relate to units that are mappable at a subregional scale. Seismic stratigraphic units on multichannel reflection data may not correspond to identifiable velocity layers, and seismic correlation is hindered anyway by numerous stacked mass transport deposits particularly beneath the slope (Mosher *et al.* 2012b). Boreholes on the Beaufort-Mackenzie shelf intersect variable lithologies and also fluid overpressures (Chen *et al.* 2010), both of which might cause low velocities. However, the interval of apparent low velocity is defined by fewer than about six samples in each subregion, so no additional layers were added to the reference models.

3.3 Station-specific velocity–depth models to map spatial trends in the model parameters and the outlying samples

Best-fitting model parameters are calculated, on a station-by-station basis, using the methodology of Section 2.3 with the value of V_∞ estimated within each given subregion. The results for 127 stations having four or more velocity samples are gridded at a 5 × 5 km interval and shown on Figs 7 and 8. The variation of V_0 across the region is clearly systematic. It averages 1.77 km s^{-1} over the slopes, 1.66 km s^{-1} over the abyssal plain of the central Canada Basin, and 1.58 km s^{-1} across the Alpha-Mendeleev magnetic domain. The total range of V_0 is from 1.40 to 1.95 km s^{-1}. The spatial variation of α is also systematic. Ranging between 0.24 and 1.88 km^{-1}, the values increase steadily from the southeast to the northwest. Within the Alpha-Mendeleev magnetic domain, the average value of α is 0.74 km^{-1}. The highest values, exceeding 0.90 km^{-1}, correspond to regions of the Alpha-Mendeleev Ridge and the northern tip of the

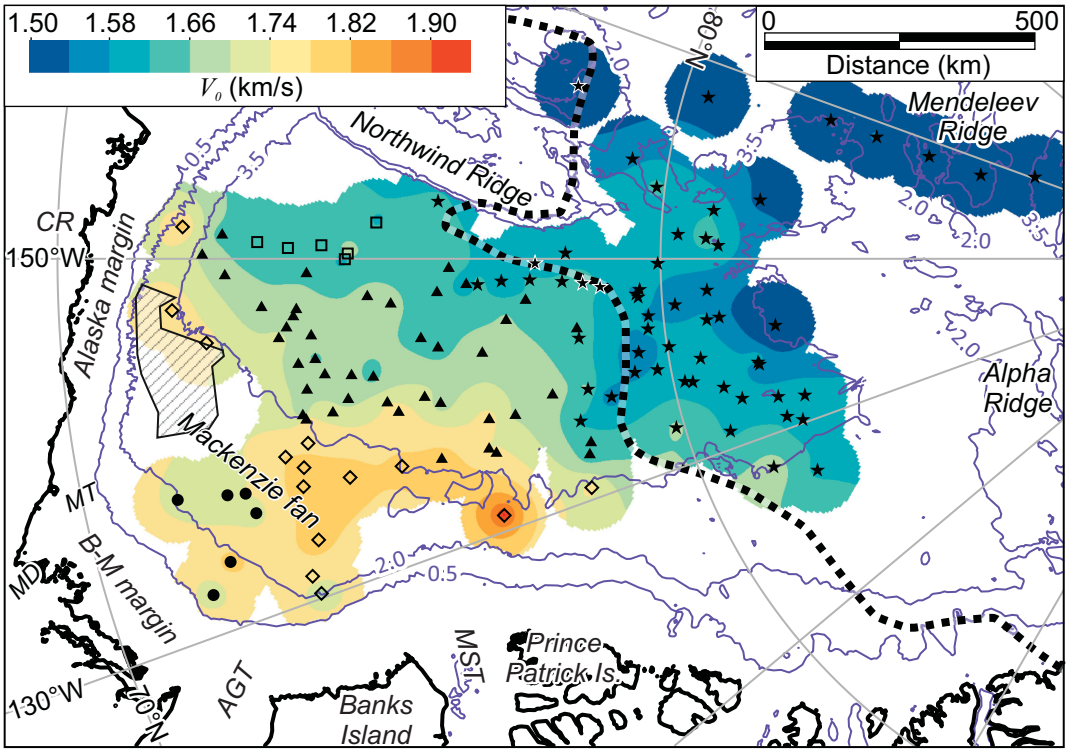

Figure 7. Map of V_0 determined from the regression models for 127 stations having at least 4 velocity–depth samples. Stations are categorized as in Fig. 5. Hatched polygon: May & Grantz (1990) study area. Dashed black line: southern boundary of the Alpha-Mendeleev (F1) magnetic domain (Saltus *et al*. 2011). Solid blue lines: 0.5, 2.0, and 3.5 km isobaths. *AGT*, Amundsen Gulf Trough; *B-M margin*, Beaufort-Mackenzie margin; *CR*, Colville River; *MST*, M'Clure Strait Trough; *MT*, Mackenzie Trough.

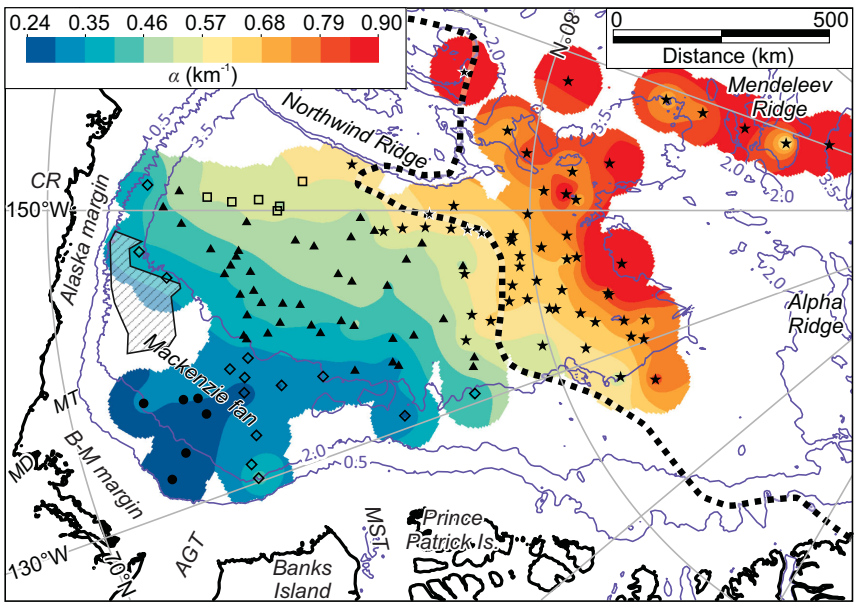

Figure 8. Map of α determined from the regression models for 127 stations having at least 4 velocity–depth samples. Stations are categorized as in Fig. 5. Hatched polygon: May & Grantz (1990) study area. Dashed black line: southern boundary of the Alpha-Mendeleev (F1) magnetic domain (Saltus *et al*. 2011). Solid blue lines: 0.5, 2.0, and 3.5 km isobaths. *AGT*, Amundsen Gulf Trough; *B-M margin*, Beaufort-Mackenzie margin; *CR*, Colville River; *MST*, M'Clure Strait Trough; *MT*, Mackenzie Trough.

Chukchi Plateau where the sedimentary succession is thinner than about 1.8 km.

The minima and maxima of the observed-to-predicted velocity ratio for each station are mapped on Figs 9 and 10, respectively. These figures illustrate how closely the outlying samples match the station-specific models. The match is within ±7 per cent for 78 of the 127 stations analysed, which demonstrates a high level of consistency in the data set produced by Chian & Lebedeva-Ivanova (2015). Depths for outlying samples that are at least 7 per cent slower or faster than the predicted velocity are annotated on the figures.

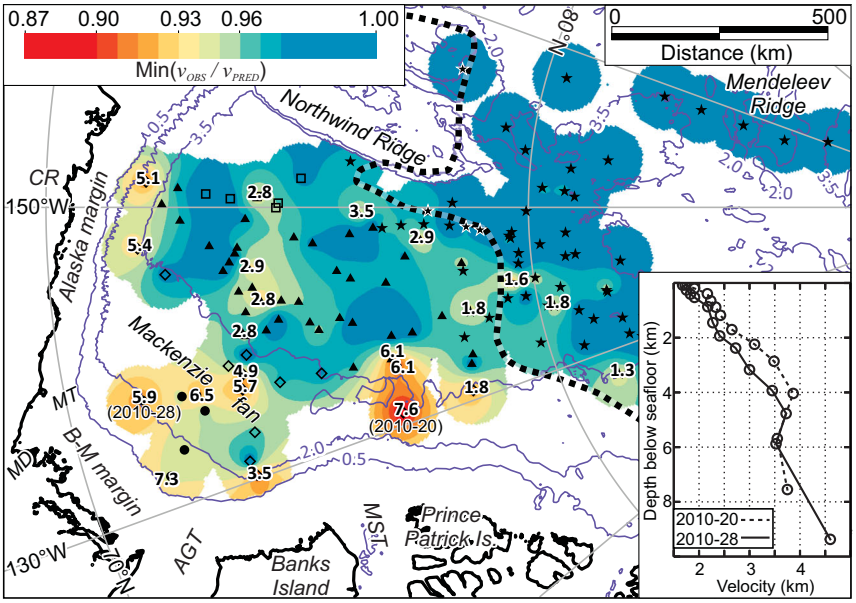

Figure 9. Minimum of the observed-to-predicted velocity at 127 stations having at least 4 samples. The depth to the anomaly below seafloor (km) is annotated at stations where the ratio is less than or equal to 0.93. The profiles for two stations at which there are apparent inversions of the observed velocity gradient with depth are shown on the inset graph. Dashed black line: southern boundary of the Alpha-Mendeleev (F1) magnetic domain (Saltus *et al*. 2011). Solid blue lines: 0.5, 2.0 and 3.5 km isobaths. *AGT*, Amundsen Gulf Trough; *B-M margin*, Beaufort-Mackenzie margin; *CR*, Colville River; *MST*, M'Clure Strait Trough; *MT*, Mackenzie Trough.

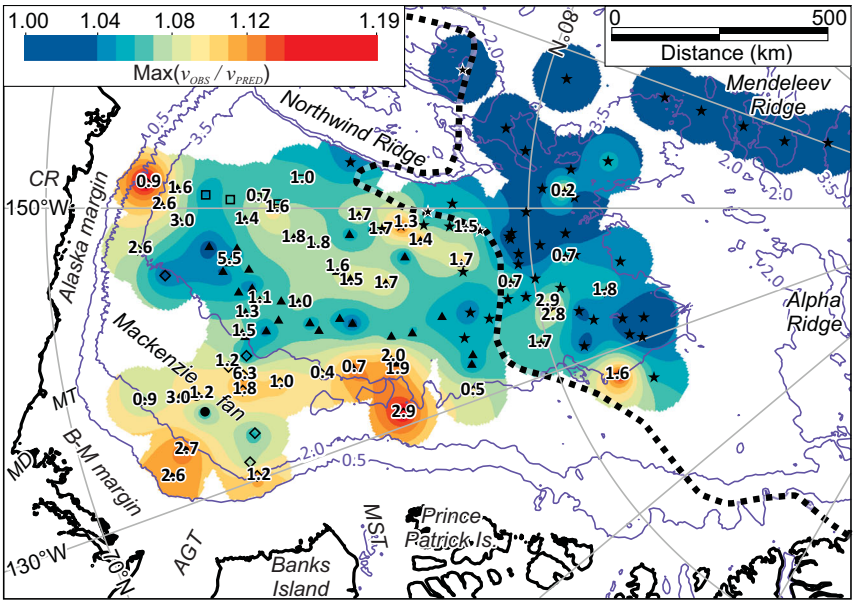

Figure 10. Maximum of the observed-to-predicted velocity at 127 stations having at least four samples. The depth to the anomaly below seafloor (km) is annotated at stations where the ratio is greater than or equal to 1.07. Dashed black line: southern boundary of the Alpha-Mendeleev (F1) magnetic domain (Saltus *et al*. 2011). Solid blue lines: 0.5, 2.0 and 3.5 km isobaths. *AGT*, Amundsen Gulf Trough; *B-M margin*, Beaufort-Mackenzie margin; *CR*, Colville River; *MST*, M'Clure Strait Trough; *MT*, Mackenzie Trough.

These outliers tend to occur at similar depths along distinct 2-D spatial trends, suggesting the influence of systematic geological factors rather than random errors in the underlying sample sets.

3.4 Determination of sedimentary thickness

The thickness of the sedimentary succession is calculated from the difference of the seafloor and base horizons in the time domain. Values for V_0 and α are assigned to each common midpoint location of the seismic reflection data using the parameter values of the nearest cell in the grids shown on Figs 7 and 8. Likewise, the value for V_∞ is assigned from the closest subregional velocity–depth model. Sedimentary thickness is then converted to depth at every common midpoint location using the methodology of Section 2.3.3. The results are shown on Fig. 11.

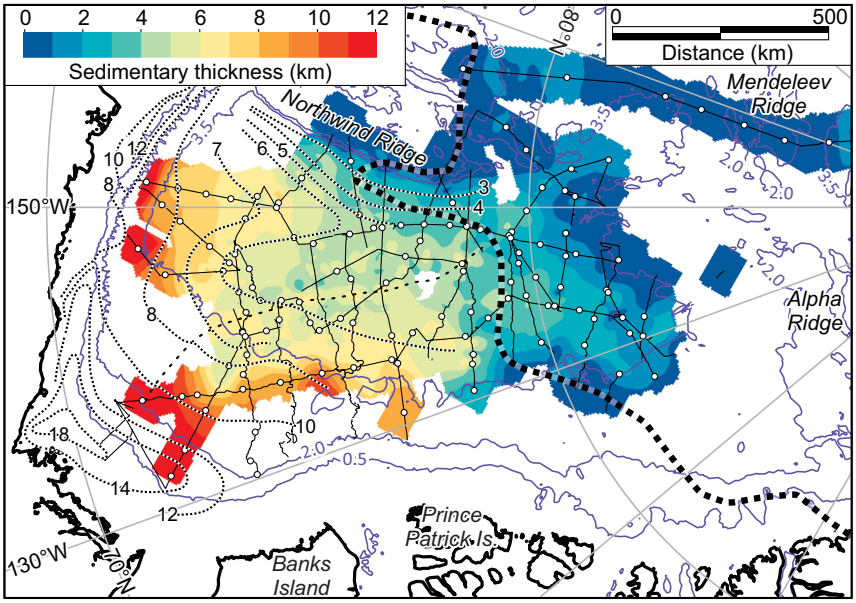

Figure 11. Thickness of the sedimentary succession. Thin solid lines: seismic reflection profiles acquired during 2007 through 2011. White dots: sonobuoy stations. Thin dotted lines: sedimentary thickness isopachs, labelled in km, from Grantz *et al*. (2011). Thin dashed black line: location of the –2.0 mGal free-air gravity anomaly interpreted as an extinct spreading axis by Grantz *et al*. (2011). Thick dashed black line: southern boundary of the Alpha-Mendeleev (F1) magnetic domain (Saltus *et al*. 2011). Solid blue lines: 0.5, 2.0 and 3.5 km isobaths.

4 DISCUSSION

The results of this study provide new sedimentary thickness information across an extensive frontier region, while also characterizing velocity–depth behaviour for a wide range of deep-water marine settings. The predominant lithologies in such settings are often siliciclastic mudrocks, including siltstones, claystones, mudstones and shales. These rocks are of global scientific and economic importance, yet their physical properties, such as seismic velocity, are understudied (Sondergeld & Rai 2011). Coarser grained lithologies might also be present in the study region as the result of mass transport, with both orogenesis and glaciation of the surrounding margins potentially generating large volumes of clastic material. The following sections explore the geological inferences that can be drawn from the velocity–depth models even though there is a lack of borehole information.

4.1 Sedimentary thickness in the Canada Basin and southern Alpha-Mendeleev Ridge

The sedimentary thickness grid shown on Fig. 11 is based interpretations of only the 2007 through 2011 seismic data set. Gaps in this grid are due to the wide spacing between seismic reflection profiles, and because data are absent for some regions. The grid does not extend to the continental shelves because the primary seafloor multiple obscures imaging of the succession in water depths shallower than about 2.5 km. Sedimentary thickness beneath the upper slope is controlled primarily by the results of Chian & Lebedeva-Ivanova (2015), with little control from the seismic reflection data. Data sets acquired recently by the petroleum industry will be useful in future studies for correlations across the upper to middle slope. Also, residual gravity anomaly data can be used to constrain extrapolations of the sedimentary thickness beyond the bounds of the seismic data coverage.

The results shown on Fig. 11 correspond reasonably with earlier reconnaissance-scale maps (Grantz *et al*. 1990, 2011; Jackson & Oakey 1990; May & Grantz 1990; Mosher *et al*. 2012c) while representing a significant improvement in accuracy and level of detail. The most significant difference occurs beneath the slope off the Alaska margin where the present study indicates the succession is 2–3 km thicker than was mapped by Grantz *et al*. (2011). The succession thins progressively with increasing distance from the Alaska, Beaufort-Mackenzie, Banks, and Prince Patrick margins. However, the thinning outboard of Alaska is more gradual, with respect to the modern bathymetry, than outboard of the other margins. For example, a sedimentary thickness of 7 km off Alaska occurs beneath a water depth of 3.8 km, whereas the same thickness of sediment off the Beaufort-Mackenzie margin occurs beneath a water depth of about 2.8 km. This depositional pattern manifests the different histories of sediment dispersal to the two areas (Grantz *et al*. 2011; Houseknecht & Bird 2011; Grantz & Hart 2012). Maximum thicknesses beneath the upper Mackenzie fan and the middle slope off Alaska are between 12 and 13 km. The 5–7 km isopachs beneath the central abyssal plain outline a roughly 45 km wide, north–south trending graben (Mosher *et al*. 2012c, fig. 3a). This graben is congruent with the curvilinear anomaly of about –2.0 mGal in the free-air gravity field that is interpreted to represent an extinct seafloor spreading axis (Grantz *et al*. 2011).

4.2 Comparisons with published data

Results from May & Grantz (1990) help to validate the velocity–depth models for subregions 1 and 2. They used stacking velocities from processing of multichannel seismic reflection data, together with a sparse compilation of seismic refraction velocities (Mair & Lyons 1981; Baggeroer & Falconer 1982), to derive measurements of interval velocity for the slope off of the Alaska margin and also a portion of the Mackenzie fan. The region studied by May & Grantz (1990) is indicated on Figs 7 and 8, and their measurements are plotted on Fig. 12 with respect to the five subregional models. The model for subregion 2—constructed explicitly for slope settings

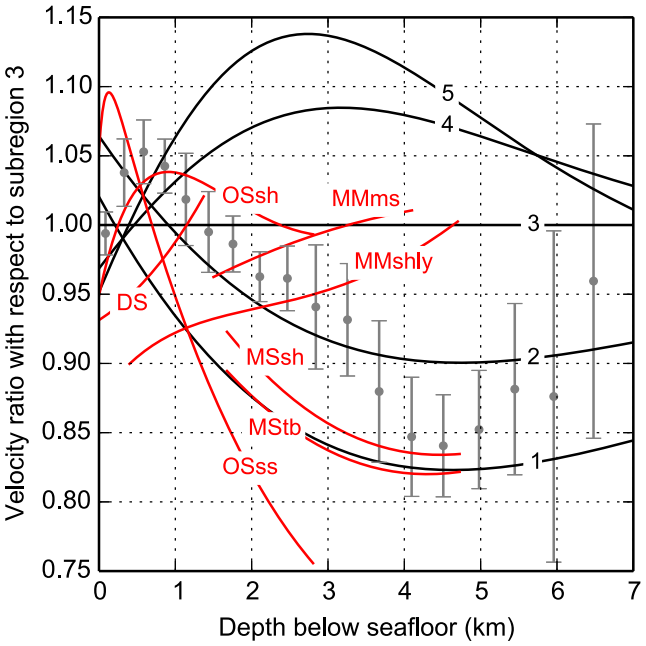

Figure 12. Comparisons between the models and published data sets. Subregional models 1 through 5 are plotted as black lines numbered 1 through 5. Grey error bars indicate interval velocities determined by May & Grantz (1990) for a lower slope region of the southern Canada Basin (indicated on Figs 7 and 8). Red lines indicate trends determined from core and borehole sonic measurements: *DS*—deep-sea, Cretaceous and younger sediments sampled by the Deep Sea Drilling Program (Carlson *et al*. 1986); *MMms*—mixed marine, Lower Jurassic mudstone formation, North Sea (Japsen 2000); *MMshly*—mixed marine, Mesozoic and Cenozoic shaley sandstones and shales, North Sea, Norwegian Shelf, and Barents Sea (Storvoll *et al*. 2005); *MStb*, mid-slope, Miocene turbidites including sheet sands and channel-levee-overbank complexes, Gulf of Mexico (Smith & Sondergeld 2001); *MSsh*, mid-slope, Miocene shales, Gulf of Mexico (Smith & Sondergeld 2001); *OSsh*, outer shelf, Plio-Pleistocene clays and shales, Gulf of Mexico (Dutta *et al*. 2009); *OSss*, outer shelf, Plio-Pleistocene sands and sandstones, Gulf of Mexico (Dutta *et al*. 2009).

of the Canada Basin—exhibits the closest overall match, and the degree of correspondence is generally within or close to the uncertainty of the measurements. There do appear to be systematic differences. For example, measurements shallower than 3.5 km are about 2.5 per cent faster than the subregion 2 model, whereas measurements between depths of 4 and 5 km are about 5 per cent slower and are in fact most similar to the subregion 1 model for the Mackenzie fan. Since an influence from the fan is probable within the region studied by May & Grantz (1990), their results are consistent with those of the present study.

Published borehole data from normally compacted, brine-saturated, clastic successions are plotted and labelled in red on Fig. 12, although comparison with these trends involves several caveats. Most of the trends are derived from sonic measurements collected over spatial scales of cm to m, rather than tens or hundreds of m as is the case for the present results. Also, core and borehole measurements may be adversely affected by expansion of the samples, drilling-induced fractures, and invasion of drilling fluids. Finally, widely varying curve-fitting methodologies are used in the various published studies and the specific choices of functional form, curve-fitting domain, and regression method will cause systematic differences between trends that could approach or even exceed the resolution of the underlying measurements. Despite these caveats, the published results do provide some context for geological interpretation.

Fully lithified, brine-saturated sandstones typically exhibit lower velocity with depth than is observed for any of the subregional models. At a depth of 2.5 km, for example, the velocity of Plio-Pleistocene outer-shelf sandstones in the eastern Gulf of Mexico (OSss; Dutta *et al*. 2009) is 6.5 per cent slower than the subregion 1 model, 23 per cent slower than the subregion 3 model, and 37 per cent slower than the subregion 5 model. In contrast, the velocity of outer-shelf shales in the same succession (OSsh; Dutta *et al*. 2009) matches the subregion 3 model to within 5 per cent for all measured depths. A similar match with the subregion 3 model exists for Lower Jurassic mixed-marine mudstones of the North Sea (MMms; Japsen 2000). Mixed-marine shaley sandstones and shales in Mesozoic–Cenozoic successions of the northern North Sea and the Norwegian Sea (MMshly; Storvoll *et al*. 2005) compare favourably with the subregion 3 model at depths greater than 2.5 km. The same trend is up to 10 per cent slower at shallower depths, which might be due to complexities in the underlying data set that was compiled by Storvoll *et al*. (2005). They used sonic measurements from a wide range of marine depositional settings in several basins with differing subsidence histories, and from both overpressured and normally-pressured intervals.

Unlithified, brine-saturated sands exhibit higher seismic velocity than do clays for a given state of consolidation (Erickson & Jarrard 1998), and this phenomenon is evident in the velocity ratio versus depth trends shown on Fig. 12. The trend for outer shelf sands (OSss; Dutta *et al*. 2009) above depths of 0.5 km is up to 15 per cent faster than any of the five subregional models. The subregion 1 and 2 models most closely resemble the OSss trend within this depth range. In comparison, the shallow subregion 3, 4 and 5 models most closely resemble the trend for Cretaceous and younger deep-sea sediments in predominantly abyssal plain and continental rise settings (DS; Carlson *et al*. 1986), which was derived using borehole-to-seismic correlations at 154 global sites of the Deep Sea Drilling Program.

The above observations suggest that sandstones are not a predominant lithology within subregions 1 through 5. However, the subregion 1 model constructed for the Mackenzie fan does closely match, to within 2.5 per cent or better, the velocity trends for mid-slope, deep-water turbidites (MStb) and mid-slope shales (MSsh) in the Miocene succession of the eastern Gulf of Mexico (Smith & Sondergeld 2001). This succession is comparable to the Mackenzie fan in terms of general depositional setting, modern water depth (2 km), and thickness (Upper Eocene to Miocene strata are up to 5-km-thick near subregion 1; Dietrich *et al*. 1989). Thus, by analogy, the predominant lithologies of subregion 1 are interpreted to be turbidite sandstones and shales. Deep-water marine shales are interpreted for subregions 2 through 5, although sandy intervals might be present within unconfined turbidites and amalgamated channel deposits.

Attempts to compare the present results with those from other regions of the Arctic Ocean were unfruitful due to the limited range and density of the published measurements. For example, the maximum sedimentary thickness tabulated by Engen *et al*. (2009) is 1.35 km, and the maximum velocity is 2.6 km s^{-1}. There is little variation between any of the five subregional velocity–depth models over this range. Likewise, borehole sonic velocities from Lomonosov Ridge collected during Expedition 302 of the Integrated Ocean Drilling Program (Moran *et al*. 2006) are all slower than 1.8 km s^{-1} and are from depths shallower than 0.2 km.

4.3 Geological interpretation of the model parameters

Seismic velocity in sedimentary rocks is a function of the elastic moduli, which are affected by numerous, often interrelated properties of the lithology, the pore fluids, and the environment. For example, considering only lithology, the following are all important factors: compaction state, burial history, age, cementation, texture, bulk density, clay content, anisotropy, fracturing, porosity, lithology and pore shape (Wang 2001). Pore fluids and environmental factors can also exert strong influence, but this discussion will focus on the lithological factors that may be relevant at a regional scale.

Some generalizations are possible if the sedimentary succession is assumed to consist of brine-saturated siliciclastic sediments and sedimentary rocks. Erickson & Jarrard (1998) found that for this case the dominant factors affecting seismic velocity are clay content and porosity, and that clay content is a negligible factor for porosities greater than the critical porosity (i.e. the transitional limit above which the sediments are essentially in suspension). Thus for sediments at or near the seafloor, an increase in porosity corresponds with a straightforward decrease in velocity. This inverse relationship holds true for more deeply buried sediments that are at less than critical porosity except that, for any given porosity, the velocity of pure sand is about 1.3 km s^{-1} faster than that of pure clay. Sand-clay mixtures exhibit intermediate velocities between the bounds for pure sand and clay. Erickson & Jarrard (1998) used an extensive compilation of core and borehole measurements to determine that the lithological effect is significant at porosities less than about 40 per cent, which provides an approximate measure of critical porosity. Critical velocity in their data set is about 2.1 km s^{-1}. They proposed a family of polynomial equations which, although probably not globally accurate (Tudge & Tobin 2013), provide a first-order approximation of the interrelationships between velocity, porosity, and lithology.

4.3.1 *Initial velocity, V_0*

The initial velocity is simply a model extrapolation to zero burial depth, so it should not be construed as an actual measurement of seafloor velocity. The extrapolation is sensitive to the distribution of velocity–depth samples from the uppermost tens to hundreds of m in the succession, so it is likely affected by the properties of both Holocene and Late Pleistocene or older strata. Nonetheless, 125 of the 127 station-specific models yield geologically plausible values for V_0 of between 1.50 and 1.95 km s^{-1}. The two minimum outlying values of 1.40 and 1.41 km s^{-1}, though possibly unreliable, are at least physically plausible. For example, Fruehn *et al*. (2008) reported low velocities of between 1.20 and 1.35 km s^{-1} for sediments within a few hundred m of the seafloor in deep-water regions offshore eastern India, which they interpreted as the result of either free-gas or water-saturated clay bodies.

V_0 increases systematically to the southeast, predominantly towards the Beaufort-Mackenzie and Banks Island margins (Fig. 7). This trend is likely due to coarsening of Quaternary sediments in this direction since distally deposited clays should have significantly higher initial porosity than either silts or sands deposited closer to the margins (Singer & Müller 1983). The highest values for V_0 occur beneath the slope off Banks Island, between the Amundsen Gulf and M'Clure Strait troughs, and a lobate pattern of V_0 greater than 1.68 km s^{-1} extends outboard of the M'Clure Strait Trough into the central Canada Basin. These observations are consistent with the variable history of Laurentide Ice Sheet advance across the Beaufort-Mackenzie and Banks Islands margins. Batchelor *et al.* (2013, 2014) provide seismic stratigraphic evidence for at least eight Quaternary ice-stream advances through the Amundsen Gulf Trough to the shelf break, where a trough-mouth fan with a minimum volume of 10 000 km^3 is present on the adjacent slope. A similar history of ice-stream advance was focussed through the M'Clure Strait Trough, resulting in deposition of an even larger trough-mouth fan of about 60 000 km^3 (Batchelor *et al*. 2014). The Amundsen Gulf and M'Clure Strait ice-streams were fed by major drainage basins of the Laurentide Ice Sheet, and they supplied significant quantities of ice and sediment to the Arctic Ocean during much of the Quaternary. In contrast, there is evidence for only two Quaternary ice-stream advances through the Mackenzie Trough which was situated at the extreme northwest ice-sheet margin and was likely fed by a smaller drainage basin (Batchelor *et al*. 2013).

4.3.2 *Final velocity, V_∞*

The final velocity provides an estimate of the bulk average matrix velocity for the entire sedimentary succession, assuming that the behaviour of velocity reduction with depth is adequately sampled. Issler (1992) reported matrix velocities of between 4.5 and 5.0 km s^{-1} for Tertiary, silt-rich shales beneath the nearby Beaufort-Mackenzie shelf. Hansen (1996) reported a value of 5.17 km s^{-1} for Cretaceous and Tertiary shales beneath the Norwegian shelf, and Japsen (2000) reported a value of 5.41 km s^{-1} for a Lower Jurassic shale unit beneath the North Sea. The matrix velocities of sandstones and carbonates are typically faster, ranging between 5.48 and 5.95 km s^{-1} in the former and between 6.40 and 7.00 km s^{-1} in the latter (Mavko *et al*. 2009). Thus, the V_∞ values determined in the present study (Fig. 6) are consistent with mudrocks being the bulk lithology in all subregions.

Various factors, such as differences in lithology or pore structure, might explain the relatively small variations of V_∞ between subregions and also the slightly lower matrix velocities reported by Issler (1992). The clastic sedimentary succession of the Beaufort-Mackenzie shelf, for example, likely has a coarser grain size distribution than the more distal succession of subregion 1. The succession is also thinner beneath the shelf, so chemical compaction may not be as significant a factor as in subregion 1. However, matrix velocity is an intrinsically difficult measurement to define in shales (Hansen 1996; Erickson & Jarrard 1998; Tudge & Tobin 2013) and it is not strictly equivalent to final velocity, which is a field-scale extrapolation based on an assumption of exponential behaviour. The small variations in the final velocity estimates may be of no physical significance, but the consistency of the estimates and their compatibility with the matrix velocities from Issler (1992) demonstrate that the velocity–depth models do generate plausible extrapolations.

4.3.3 *Exponential decay constant, α*

The reduction of porosity with depth is strongly affected by lithology. For example, Hölzel *et al*. (2008) compiled the following values for the exponential porosity decay constant (km^{-1}) from five published studies: dolomite, 0.16; quartz sandstone, 0.36; shaley sandstone, 0.39; shale, 0.40–0.51; calcite, 0.54 and chalk, 0.47–0.71. These values can be compared directly with the modelled exponential decay constant, α (Fig. 8), assuming that the relationship between seismic velocity and porosity is linear, as in the time average equation of Wyllie *et al*. (1956). This is a heuristic assumption that is accurate only under limited conditions (Mavko *et al*. 2009), but it does allow an approximate frame of reference to be constructed.

The systematic decrease of α towards the Beaufort-Mackenzie margin (Fig. 8) is consistent with an increasing bulk sandstone-to-shale ratio in that direction. Indeed, in the upper to middle slope, the lobate pattern formed by the $\alpha = 0.30\,\mathrm{km}^{-1}$ isoline is suggestive of deposition in a deep-water fan (Fig. 8). Further downslope, the isolines for α between 0.35 and $0.46\,\mathrm{km}^{-1}$ broadly parallel the Mackenzie fan bathymetry, but not the bathymetry of the Alaska and Prince Patrick Island margin segments. Thus, the Mackenzie drainage system seems to be a strong factor in the spatial distribution of α, which provides independent confirmation that it is the predominant sedimentary source.

Further northward, the isolines for $\alpha > 0.46\,\mathrm{km}^{-1}$ parallel the Alpha-Mendeleev magnetic domain. Within subregions 4 and 5, α exceeds the maximum value of the porosity decay constant for shale, as reported by Hölzel *et al*. (2008; Figs 6 and 8). Furthermore, the upper quartile of α for stations in subregion 5 exceeds even the highest porosity decay constant for chalk. At burial depths of 1.5–4.4 km, the subregion 4 and 5 models are 7–14 per cent faster than the abyssal plain mudrocks characterized by the subregion 3 model (Fig. 12). Finally, between subregions 3 and 5, the spatial transition to higher velocities occurs across a distance of a few tens of km at most (Fig. 5, inset graph). It seems likely that the high velocities of subregions 4 and 5 are the result of more than just systematic changes in lithology.

4.4 Spatial trends in the outlying velocity–depth samples

The most extreme low-velocity outliers of the region, in some cases 10–13 per cent slower than predicted, occur chiefly at burial depths of greater than 5 km and they are located along the middle to lower slope (Fig. 9). At two stations in the slope region (2010–20 and 2010–28) there are even inversions in the gradient of the measured velocity with depth (Fig. 9, inset graph). Chian & Lebedeva-Ivanova (2015) interpreted and modelled low-velocity layers at these stations based on sharp jumps in the first arrivals of the observed refracted phases. These are preliminary analyses, so further work is required to verify the existence of the low-velocity layers and their possible significance. Nonetheless, the low-velocity outliers beneath the slope are associated with intervals that are tens to hundreds of metres in thickness. They occur, with two exceptions, at depths of 5 to 7 km along margin segments that are separated by hundreds of km, and they occur outboard of major sediment sources where the average sedimentation rates are high (the Mackenzie Delta, the Colville River, and the M'Clure Strait Trough). These observations suggest that the low-velocity outliers beneath the slope are caused by undercompaction rather than to discrete changes in lithology. Excess pore pressures are common beneath the Beaufort-Mackenzie shelf at burial depths ranging from less than 1 km to greater than 5 km (Chen *et al*. 2010), and perhaps this phenomenon extends beneath the slope.

Coherent trends in the low-velocity outliers, some up to 7 per cent slower than predicted, occur beneath the abyssal plain at depths averaging about 2.8 km, and also shallower at about 1.7 km (Fig. 9). These trends are perhaps related to lithology. For example, stacked sequences of sandy turbidites could be envisioned for the trend extending distally from the Mackenzie fan. Undercompaction is also plausible since the diagenetic transformation of smectite to illite often causes excess pore fluid pressures, and the transformation generally occurs at 2–3 km burial depth where the temperatures are between 70 and 100 °C (Storvoll *et al*. 2005).

The most extreme high-velocity outliers of the region are 12–19 per cent faster than predicted and they occur beneath the middle to lower slope, much like the most extreme low-velocity outliers. However, the high velocities are at shallower burial depths of 1–3 km (Fig. 10) within presumably Pliocene and younger strata. They might be associated with concentrations of relatively coarse sediment contributed by glacial erosion of the surrounding margins. The high-velocity outliers beneath the abyssal plain are 7–10 per cent faster than predicted and they occur at an average burial of 1.5 km. They could be caused by calcareous or siliceous oozes, which are often widespread in pelagic settings.

4.5 Associations with geothermal heat flow and crustal type

More than 130 observations of heat flow at the seafloor are summarized for the region in several published studies (Lachenbruch & Marshall 1969; Taylor *et al*. 1986; Langseth *et al*. 1990), although fewer than a quarter of these observations have been reported in detail (Louden *et al*. 1990). The most recent compilation by Langseth *et al*. (1990) includes averaged measurements from the seven geographic areas labelled A to G on the magnetic anomaly map given in Fig. 13. Crustal types identified by Grantz *et al*. (2011) are also annotated on this map. Heat flow values for areas B, C, D and G exhibit little scatter about their grouped average, which is $56\,\mathrm{mW\,m}^{-2}$. In comparison, heat flow is higher in areas A and E, and lower in area F. However there is only one measurement in area A, making it difficult to judge its accuracy, and hummocky terrain in area F may cause a heat flow reduction of $1–3\,\mathrm{mW\,m}^{-2}$ (Langseth *et al*. 1990). Only the measurements from area E reliably indicate a significant deviation from the average heat flow. Thus, there are no discernible associations between heat flow and sedimentary thickness even though the latter varies by a factor of up to ten between the various heat flow areas (Fig. 11).

The F1 magnetic domain of Saltus *et al*. 2011 outlines a chaotic pattern of magnetic anomalies with absolute magnitudes greater than about 256 nT (Fig. 13), and it is associated with the Alpha-Mendeleev large igneous province. Lithological factors related to widespread magmatism in this province might be linked to the elevated seismic velocities. For example, high concentrations of smectite are often associated with mafic volcanism. From published field-scale studies though, this mineral is associated with reductions in seismic velocity rather than increases (Storvoll *et al*. 2005). Another possibility is that high-velocity volcanic units could be incorporated within the sedimentary succession. Using seismic reflection and refraction data, Bruvoll *et al*. (2012) interpreted the existence of multiple lava flows over voluminous tuff deposits and/or possible sediments along Mendeleev and northwestern Alpha ridges. However, the results for subregion 5 in the present study demonstrate that the velocity–depth samples associated with the Alpha-Mendeleev magnetic domain are faster than the regional average throughout the bulk of the succession (Fig. 6). No evidence has been found at a subregional scale for discrete sedimentary units exhibiting high velocity.

A more promising hypothesis is that episodic high palaeo-heat flow in the Alpha-Mendeleev large igneous province might have accelerated porosity reduction through chemical compaction processes, thereby increasing the average velocity of the bulk succession. A possible example of such a phenomenon in the Newfoundland Basin is described by Karner & Shillington (2005). Using results from the Ocean Drilling Program Leg 210, they

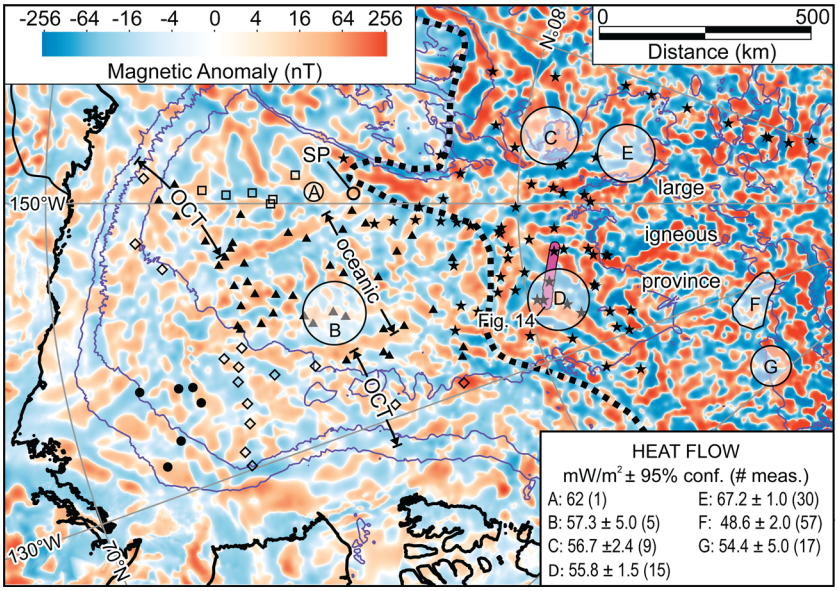

Figure 13. Magnetic anomaly map with crustal affinities interpreted by Grantz *et al*. (2011). Velocity stations are categorized as in Fig. 5. Mean heat flow values compiled by Langseth *et al*. (1990) are annotated in mW m^{-2} for areas A through G. The magnetic anomaly grid is from Gaina *et al*. (2011). Dashed black line: southern boundary of the Alpha-Mendeleev (F1) magnetic domain (Saltus *et al*. 2011). Solid blue lines: 0.5, 2.0 and 3.5 km isobaths. OCT, ocean–continent transitional crust; SP, possible serpentinized peridotite.

determined that two diabase sills within Aptian sediments were emplaced 100–200 m above transitional crust across an area of roughly 150 × 600 km^2. Vitrinite reflectance and palynomorph data from Site 1276 indicate that thermal alteration affected the sediments only within about 20 m of the sills (Pross *et al*. 2007). However, Peron-Pinvidic *et al*. (2010) found evidence from borehole and seismic reflection data that hydrothermal venting affected more than 500 m of the overlying succession, raising the possibility that fluid flow and heat advection accelerated chemical compaction processes without substantially altering other indicators of thermal maturity. Karner & Shillington (2005) reported an exponential decay constant of 0.85 km^{-1} for the claystones, mudstones, and siltstones at Site 1276, which clearly exceeds the range of 0.40–0.51 km^{-1} for shales (Hölzel *et al*. 2008). It also compares favourably with the values of α determined for many of the stations in subregion 5 (Fig. 8).

Numerous volcanic edifices comprise the Alpha-Mendeleev large igneous province, and sills or dykes are also likely to be present considering that magmatism persisted until at least the Late Cretaceous (Jokat *et al*. 2013). It is worth noting also that Langseth *et al*. (1990) interpreted the relatively high heat flow in area E (Fig. 13) as evidence for extensional tectonics during the early Palaeogene, raising the possibility of post-Cretaceous magmatism. An example of a buried volcanic edifice within the large igneous province is illustrated by the seismic reflection profile on Fig. 14 (see Fig. 13 for location). The three-dimensional morphology of the edifice is unknown since it is crossed by only one seismic profile, but the associated magnetic anomalies indicate that the edifice may form a northeast trending ridge or seamount (Fig. 13). Semi-continuous reflectivity in the upper crystalline crust beneath the interpreted sedimentary succession may indicate the base of volcanic flow units. A highly reflective unit, interpreted as a sill complex in the lower sedimentary succession, exhibits seismic impedance contrasts that are in some places comparable to that of the seafloor. The unit comprises a series of five parallel continuous reflections apparently emanating from the flanks of the volcanic edifice, which thin westward to just two parallel reflections (Fig. 14b). These reflections exhibit km-scale saucer-shaped relief between flat segments of up to 5 km in length and occasional Y-shaped terminations. The position of this unit in the lower sedimentary succession, its current depth of burial, and the overall seismic facies are similar to those features of the sill complex in the Newfoundland Basin, as described by Karner & Shillington (2005).

5 CONCLUSIONS

(1) Seismic velocity within the sedimentary succession of the Canada Basin and southern Alpha-Mendeleev Ridge is characterized by a single-layer, exponential model of inverse velocity versus depth in which the parameters are allowed to vary spatially. The observed-to-predicted velocity ratio is within ±7 per cent for 78 out of the 127 stations analysed, which demonstrates a high level of consistency in the underlying data set of Chian & Lebedeva-Ivanova (2015).

(2) Distinctive velocity–depth behaviours are documented for the Mackenzie fan, the continental slopes beyond the Mackenzie fan, the abyssal plain, the southwestern Canada Basin, and the Alpha-Mendeleev magnetic domain.

(3) The sedimentary prism along the rifted margins of Arctic North America has a thickness of 12–13 km beneath the upper Mackenzie fan and middle slope off of Alaska. The prism thins more gradually outboard of the Alaska margin than outboard of the Beaufort-Mackenzie margin even though the continental terrace of the latter is wider, which manifests different histories of sediment dispersal to the two areas.

(4) The spatial distribution of initial velocity (V_0) is consistent with interpreted coarsening of Quaternary sediments towards the Beaufort-Mackenzie and Banks Island margins. Furthermore, the coarsest Quaternary sediments are interpreted to occur within a depositional lobe between the Amundsen Gulf and M'Clure Strait troughs that extends into the central Canada Basin. This finding is consistent with the variable history of Laurentide Ice Sheet advance across the Beaufort-Mackenzie and Banks Island margins.

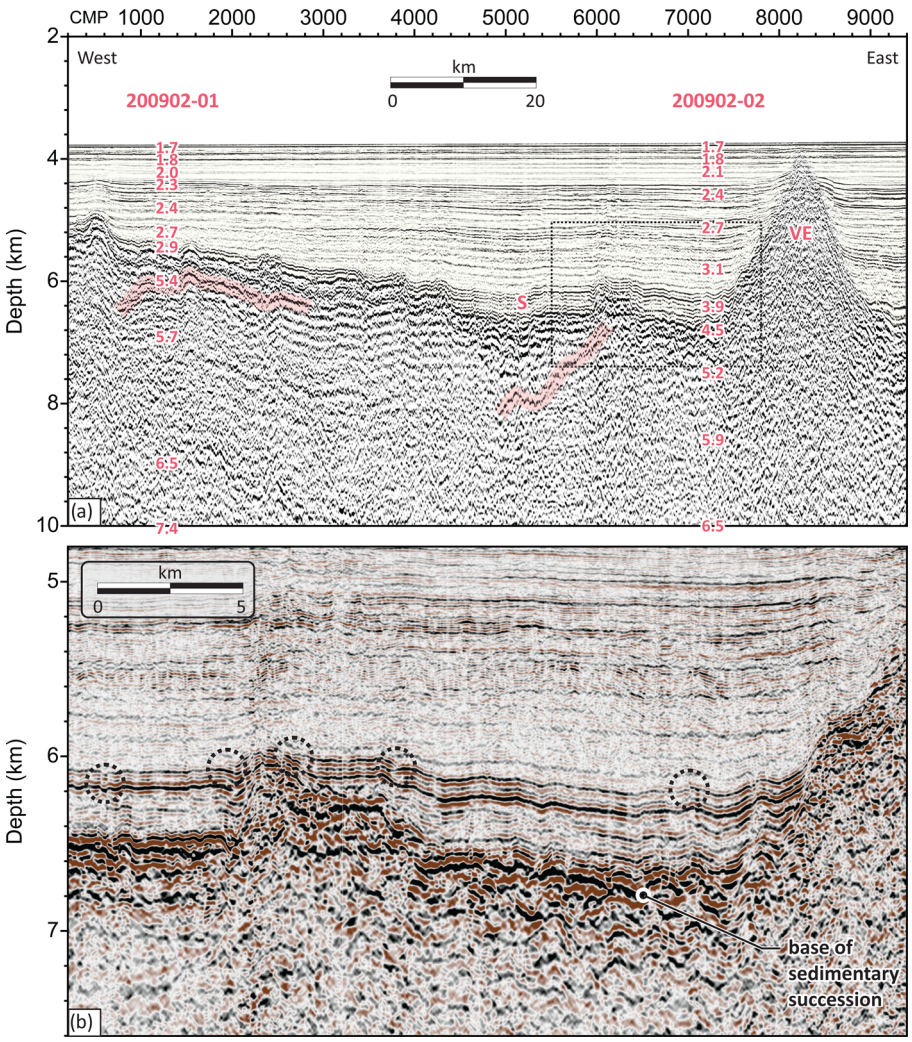

Figure 14. (a) Seismic reflection profile LSL0902, depth-converted as described in Section 3.4. (location shown on Fig. 13). The sedimentary succession is highlighted in yellow, and upper crustal reflections, possibly indicating interfaces within volcanic flow units, are marked in pink. Average interval velocities from Chian & Lebedeva-Ivanova (2015) are annotated in km s^{-1}. Dashed box, interval shown on (b); S, interpreted sill unit; VE, volcanic edifice. (b) Enlarged image of the interpreted sill unit emanating from the western flank of the volcanic edifice. Dashed circles, abrupt Y-shaped reflection terminations possibly indicating sill injections within the sedimentary succession.

(5) The values of final velocity (V_∞) obtained for all subregions indicate that the succession is dominated by mudrocks, and this interpretation is supported by comparisons with published borehole data. The subregion 1 model constructed for the Mackenzie fan closely matches, to within 2.5 per cent or better, velocity trends for Miocene turbidites and shales beneath the middle slope of the eastern Gulf of Mexico. Deep-water marine shales are interpreted for subregions 2 through 5, although sandy intervals might be present within unconfined turbidites and amalgamated channel deposits.

(6) Using published values as an approximate frame of reference, the systematic decrease of the porosity decay constant (α) towards the Mackenzie Delta is consistent with an increase in the bulk sand-to-shale ratio in this direction, supporting the inference that the Mackenzie drainage system was the predominant source of siliclastic sediments to the basin.

(7) Systematic changes in lithology are unlikely to fully account for the high values of α and the prominent increases in velocity that are associated with the southwestern Canada Basin and the Alpha-Mendeleev magnetic domain (subregions 4 and 5). Accelerated porosity reduction due to elevated palaeo-heat flow is inferred for these regions, which may be related to the underlying crustal types or possibly volcanic intrusion of the sedimentary succession.

(8) Spatially coherent trends in the minimum outlying samples occur below the middle to lower slope, generally at burial depths greater than 5 km, and also beneath the abyssal plain at shallower depths of about 2.8 and 1.7 km. Likewise, coherent trends in the maximum outlying samples are present at 2.5–3.0 km beneath the slope and about 1.5 km beneath the abyssal plain. These trends are readily interpreted in terms of the lithologies and compaction-related processes that are plausible for the given depositional settings and burial depths.

ACKNOWLEDGEMENTS

The authors gratefully acknowledge the constructive feedback provided by Charlotte Keen, Gordon Oakey, and David Piper who reviewed early versions of this manuscript. Valuable suggestions were

provided also by Harold Brekke, Richard Haworth, Alain Murphy, and Jacob Verhoef. We thank external reviewers Thomas Funck, Wilfried Jokat, and Richard Saltus for providing detailed and helpful comments. This is GSC Contribution No. 20140437.

REFERENCES

Al-Chalabi, M., 1997a. Instantaneous slowness versus depth functions, *Geophysics,* **62**(1), 270–273.

Al-Chalabi, M., 1997b. Time-depth relationships for multilayer depth conversion, *Geophys. Prospect.,* **45,** 715–720.

Athy, L., 1930. Compaction and oil migation, *Am. Assoc. Pet. Geol. Bull.,* **14,** 25–35.

Baggeroer, A. & Falconer, R., 1982. Array refraction profiles and crustal models of the Canada basin, *J. geophys. Res.,* **87**(B7), 5461–5476.

Bahr, D., Hutton, E., Syvitski, J. & Pratson, L., 2001. Exponential approximations to compacted sediment porosity profiles, *Comput. Geosci.,* **27,** 691–700.

Batchelor, C., Dowdeswell, J. & Pietras, J., 2013. Variable history of Quaternary ice-sheet advance across the Beaufort Sea Margin, Arctic Ocean, *Geology,* **41**(2), 131–134.

Batchelor, C.L., Dowdeswell, J.A. & Pietras, J.T., 2014. Evidence for multiple Quaternary ice advances and fan development from the Amundsen Gulf cross-shelf trough and slope, Canadian Beaufort Sea margin, *Mar. Pet. Geol.,* **52,** 125–143.

Bjørlykke, K., 1999. Principal aspects of compaction and fluid flow in mudstones, in *Muds and Mudstones: Physical and Fluid Flow Properties*, Special Publications, Vol. 158, pp. 73–78, eds Aplin, A., Fleet, A. & Macquaker, J., Geological Society of London.

Bruvoll, V., Kristoffersen, Y., Coakley, B., Hopper, J., Planke, S. & Kandilarov, A., 2012. The nature of the acoustic basement on Mendeleev and northwestern Alpha ridges, Arctic Ocean, *Tectonophysics,* **514–517,** 123–145.

Buchan, K. & Ernst, R., 2006. Giant dyke swarms and the reconstruction of the Canadian Arctic islands, Greenland, Svalbard and Franz Josef Land, in *Dyke Swarms: Time Markers of Crustal Evolution*, pp. 27–48, eds Hanski, E., Mertanen, S., Rämö, T. & Vuollo, J., Taylor & Francis Group.

Carlson, R., Gangi, A. & Snow, K., 1986. Empirical reflection travel time versus depth and velocity versus depth functions for the deep-sea sediment column, *J. geophys. Res.,* **91**(B8), 8249–8266.

Chen, Z., Issler, D., Osadetz, K. & Grasby, S., 2010. Pore pressure patterns in Tertiary successions and hydrodynamic implications, Beaufort-Mackenzie Basin, Canada, *Bull. Can. Petrol. Geol.,* **58,** 3–16.

Chian, D. & Lebedeva-Ivanova, N., 2015. Atlas of sonobuoy velocity analyses, Canada Basin, Open File 7661, Geological Survey of Canada, Ottawa, Canada.

Davies, A., Kemp, A. & Pike, J., 2009. Late Cretaceous seasonal ocean variability from the Arctic, *Nature,* **460,** 254–259.

Dietrich, J., Coflin, K., Lane, L., Dixon, J. & Cook, F., 1989. Interpretation of deep seismic reflection data, Beaufort Sea, Arctic Canada, Open File 2106, Geological Survey of Canada, Ottawa, Canada.

Døssing, A., Jackson, H., Matzka, J., Einarsson, I., Rasmussen, T., Olesen, A. & Brozena, J., 2013. On the origin of the Amerasia Basin and the High Arctic Large Igneous Province—results of new aeromagnetic data, *Earth planet. Sci. Lett.,* **363,** 219–230.

Drachev, S. & Saunders, A., 2003. The early Cretaceous Arctic LIP: its geodynamic setting and implications for Canada Basin opening, in *Fourth International Conference on Arctic Margins,* Dartmouth, Nova Scotia, Canada, September 30-October 3, 2003. OCS Study MMS 2006–003, pp. 206–215, eds Scott, R. & Thurston, D., U.S. Department of the Interior.

Dutta, T., Mavko, G., Mukerji, T. & Lane, T., 2009. Compaction trends for shale and clean sandstone in shallow sediments, Gulf of Mexico, *Leading Edge,* **28,** 590–596.

Engen, Ø, Gjengedal, J., Faleide, J., Kristoffersen, Y. & Eldholm, O., 2009. Seismic stratigraphy and sediment thickness of the Nansen Basin, Arctic Ocean, *Geophys. J. Int.,* **176**(3), 805–821.

Erickson, S. & Jarrard, R., 1998. Velocity-porosity relationships for water-saturated siliciclastic sediments, *J. geophys. Res.,* **103,** 30 385–30 406.

Etris, E., Crabtree, N., Dewar, J. & Pickford, S., 2001. True depth conversion: more than a pretty picture, Canadian Society of Exploration Geophysicists, *Recorder,* **26,** 11–22.

Fowler, A. & Yang, X., 1998. Fast and slow compaction in sedimentary basins, *SIAM J. Appl. Math.,* **59**(1), 365–385.

Fruehn, J., Jones, I.F., Valler, V., Sangvai, P., Biswal, A. & Mathur, M., 2008. Resolving near-seabed velocity anomalies; deep water offshore eastern India, *Geophysics,* **73**(5, Suppl.), VE235–VE241.

Gaina, C., Werner, S., Saltus, R. & Maus, S. & the CAMP-GM group, 2011. Arctic mapping project: new magnetic and gravity anomaly maps of the Arctic, in *Arctic Petroleum Geology*, Memoir No. 35, pp. 39–48, eds Spencer, A., Embry, A., Gautier, D., Stoupakova, A. & Sørensen, K., Geological Society of London.

Grantz, A. & Hart, P., 2012. Petroleum prospectivity of the Canada Basin, Arctic Ocean, *Mar. Pet. Geol.,* **30**(1), 126–143.

Grantz, A., May, S., Tayler, P. & Lawver, L., 1990. Chapter 22: Canada Basin, in *The Arctic Ocean Region, The Geology of North America,* Vol. L, pp. 379–402, eds Grantz, A., Johnson, L. & Sweeney, J., Geological Society of America.

Grantz, A., Scott, R., Drachev, S., Moore, T. & Valine, Z., 2011. Chapter 2: Sedimentary successions of the Arctic Region (58–64° to 90°N) that may be prospective for hydrocarbons, in *Arctic Petroleum Geology*, Memoir No. 35, pp. 17–37, eds Spencer, A., Embry, A., Gautier, D., Stoupakova, A. & Sørensen, K., Geological Society of London.

Hansen, S., 1996. A compaction trend for Cretaceous and Tertiary shales on the Norwegian Shelf based on sonic transit times, *Petrol. Geosci.,* **2,** 159–166.

Hegewald, A. & Jokat, W., 2013. Tectonic and sedimentary structures in the northern Chukchi region, Arctic Ocean, *J. geophys. Res.,* **118,** 3285–3296.

Hölzel, M., Faber, R. & Wagreich, M., 2008. DeCompactionTool: software for subsidence analysis including statistical error quantification, *Comput. Geosci.,* **34,** 1454–1460.

Houseknecht, D. & Bird, K., 2011. Chapter 34: geology and petroleum potential of the rifted margins of the Canada Basin, in *Arctic Petroleum Geology,* Memoir No. 35, pp. 509–526, eds Spencer, A., Embry, A., Gautier, D., Stoupakova, A. & Sørensen, K., Geological Society of London.

Hutchinson, D., Jackson, H., Shimeld, J., Chapman, C., Childs, J., Funck, T. & Rowland, R., 2009. Marine geophysical data acquisition over Canada Basin, Arctic Ocean, *EOS, Trans. Am. geophys. Un.,* **90**(23), 197–204.

Issler, D., 1992. A new approach to shale compaction and stratigraphic restoration, Beaufort-Mackenzie Basin and Mackenzie Corridor, northern Canada, *Am. Assoc. Petrol. Geol. Bull.,* **76**(8), 1170–1189.

Jackson, H., Biggar, J., Chapman, B., Shimeld, J., Hutchinson, D. & Nishino, S., 2009. Executive Summary, in *2008 Louis S. St-Laurent Field Report*, pp. 1–3, Open File 6275, eds Jackson, H.R. & DesRoches, K.J., Geological Survey of Canada, Ottawa, Canada.

Jackson, H. & Oakey, G., 1990. Plate 5, Sedimentary thickness map of the Arctic Ocean, in *The Arctic Ocean Region, The Geology of North America,* Vol. L, eds Grantz, A., Johnson, L. & Sweeney, J., Geological Society of America.

Jackson, H. *et al.*, 2008. Summary: cruise 2007 Louis S. St-Laurent, in *Field Report for the 2007 CCGS Louis S. St-Laurent Seismic Cruise to the Canada Basin*, pp. 3–4, Open File 5818, Geological Survey of Canada.

Jakobsson, M. *et al.*, 2012. The International Bathymetric Chart of the Arctic Ocean (IBCAO) Version 3.0, *Geophys. Res. Lett.,* **39,** L12609, doi:10.1029/2012GL052219.

Jakobsson, M., Grantz, A., Kristoffersen, Y. & Macnab, R., 2003. Physiographic provinces of the Arctic Ocean seafloor, *Geol. Soc. Am. Bull.,* **115**(12), 1443–1455.

Japsen, P., 2000. Investigation of multi-phase erosion using reconstructed shale trends based on sonic data. Sole Pit axis, North Sea, *Global Planet Change,* **24,** 189–210.

Japsen, P., Mukerji, T. & Mavko, G., 2007. Constraints on velocity-depth trends from rock physics models, *Geophys. Prospect.,* **55,** 135–154.

Jokat, W., Ickrath, M. & O'Connor, J., 2013. Seismic transect across the Lomonosov and Mendeleyev Ridges: constraints on the geological

evolution of the Amerasia Basin, Arctic Ocean, *Geophys. Res. Lett.,* **40**(19), 5047–5051.

Karner, G. & Shillington, D., 2005. Basalt sills of the U reflector, Newfoundland Basin: a serendipitous dating technique, *Geology,* **33,** 985–988.

Lachenbruch, A. & Marshall, B., 1969. Heat flow in the Arctic, *J. Arctic Inst. N. Am.,* **22,** 300–311.

Langseth, M., Lachenbruch, A. & Marshall, B., 1990. Chapter 9: geothermal observations in the Arctic region, in *The Arctic Ocean Region, The Geology of North America,* Vol. L, pp. 133–151, eds Grantz, A., Johnson, L. & Sweeney, J., Geological Society of America.

Lawver, L. & Scotese, C., 1990. Chapter 31: a review of tectonic models for the evolution of the Canada Basin, in *The Arctic Ocean Region, The Geology of North America,* Vol. L, pp. 593–618, eds Grantz, A., Johnson, L. & Sweeney, J., Geological Society of America.

Louden, K., Leger, G. & Hamilton, N., 1990. Marine Heat Flow Observations on the Canadian Arctic Continental Shelf and Slope, *Mar. Geol.,* **93,** 267–288.

Magara, K., 1978. *Compaction and Fluid Migration–Practical Petroleum Geology,* Elsevier.

Maher, H., Jr., 2001. Manifestations of the Cretaceous High Arctic Large Igneous Province in Svalbard, *J. Geol.,* **109**(1), 91–104.

Mair, J. & Lyons, J., 1981. Crustal structure and velocity anisotropy beneath the Beaufort Sea, *Can. J. Earth Sci.,* **18**(4), 724–741.

Mavko, G., Mukerji, T. & Dvorkin, J., 2009. *The Rock Physics Handbook,* 2nd edn, Cambridge Univ. Press.

May, S. & Grantz, A., 1990. Sediment thickness in the southern Canada Basin, *Mar. Geol.,* **93,** 331–347.

Miller, E., Gehrels, G., Pease, V. & Sokolov, S., 2010. Stratigraphy and U-Pb detrital zircon geochronology of Wrangel Island, Russia: implications for Arctic paleogeography, *Am. Assoc. Petrol. Geol. Bull.,* **94,** 665–692.

Moran, K. *et al.*, 2006. The Cenozoic palaeoenvironment of the Arctic Ocean, *Nature,* **441**(7093), 601–605.

Mosher, D. *et al.*, 2013. High Arctic marine geophysical data acquisition, *Leading Edge,* **32,** 524–536.

Mosher, D., Biggar, J., Pederson, R., Hutchinson, D., Eert, J., Netcheva, S. & Chapman, B., 2012a. Chapter 1, in *2011 Canadian High Arctic Seismic Expedition: CCGS Louis S. St-Laurent Expedition Report*, pp. 1–52, Open File 7053, Geological Survey of Canada, Ottawa, Canada.

Mosher, D., Shimeld, J. & Chapman, C., 2011. 2010 Canada Basin seismic reflection and refraction survey, western Arctic Ocean: CCGS Louis S. St-Laurent expedition report, Open File 6720, Geological Survey of Canada, Ottawa, Canada.

Mosher, D., Shimeld, J. & Hutchinson, D., 2009. 2009 Canada Basin seismic reflection and refraction survey, western Arctic Ocean: CCGS Louis S. St-Laurent expedition report, Open File 6343, Geological Survey of Canada, Ottawa, Canada.

Mosher, D., Shimeld, J., Hutchinson, D., Chian, D., Lebedeva-Ivanova, N. & Jackson, H., 2012c. Canada Basin Revealed, in *Extended Abstracts of the Arctic Technology Conference*, pp. 23 797-1–23 797-11, Offshore Technology Conference, Houston, Texas.

Mosher, D., Shimeld, J., Hutchinson, D., Lebedeva-Ivanova, N. & Chapman, C., 2012b. Chapter 13, Submarine Landslides in Arctic Sedimentation, in *Submarine Mass Movements and Their Consequences*, pp. 147–157, eds Yamada, Y., Kawamura, K., Ikehara, K., Ogawa, Y., Urgeles, R., Mosher, D., Chaytor, J. & Strasser, M., Springer Science + Business Media.

Mudie, P. & Blasco, S., 1985. Lithostratigraphy of the CESAR cores, in *Initial Geological Report on CESAR—the Canadian Expedition to Study the Alpha Ridge,* Arctic Ocean, pp. 59–99, Paper 84–22, eds Jackson, H.R., Mudie, P.J. & Blasco, S.M., Geological Survey of Canada, Ottawa, Canada.

Ostenso, N., 1962. Geophysical investigations of the Arctic Ocean Basin, Research Report No. 4, University of Wisconsin, Department of Geology, Madison, Wisconsin, U.S.A.

Peron-Pinvidic, G., Shillington, D. & Tucholke, B., 2010. Characterization of sills associated with the U reflection on the Newfoundland margin: evidence for widespread early post-rift magmatism on a magma-poor rifted margin, *Geophys. J. Int.,* **182,** 113–136.

Press, W., Teuolsky, S., Vetterling, W. & Flannery, B., 1992. *Numerical Recipes in C–The Art of Scientific Computing,* 2nd edn, Cambridge Univ. Press.

Pross, J., Pletsch, T., Shillington, D., Ligouis, B., Schellenberg, F. & Kus, J., 2007. Thermal alteration of terrestrial palynomorphs in mid-Cretaceous organic-rich mudstones intruded by an igneous sill (Newfoundland Margin, ODP Hole 1276A), *Int. J. Coal Geol.,* **70,** 277–291.

Revil, A., Grauls, D. & Brévart, O., 2002. Mechanical compaction of sand/clay mixtures, *J. geophys. Res.,* **107**(B11), 1–15.

Saltus, R., Miller, E., Gaina, C. & Brown, P., 2011. Chapter 4: regional magnetic domains of the Circum-Arctic: a framework for geodynamic interpretation, in *Arctic Petroleum Geology*, Memoir No. 35, pp. 49–60, eds Spencer, A., Embry, A., Gautier, D., Stoupakova, A. & Sørensen, K., Geological Society of London.

Sclater, J. & Christie, P., 1980. Continental stretching: an explanation of the post-Mid-Cretaceous subsidence of the central North Sea basin, *J. geophys. Res.,* **85**(B7), 3711–3739.

Singer, A. & Müller, G., 1983. Chapter 3: Diagenesis in argillaceous sediments, in *Developments in Sedimentology, Diagenesis in Sediments and Sedimentary Rocks, 2,* Vol. 25B, pp. 115–212, eds Larsen, G. & Chilingar, G., Elsevier.

Smith, T. & Sondergeld, C., 2001. Examination of AVO responses in the eastern deepwater Gulf of Mexico, *Geophysics,* **66**(6), 1864–1876.

Smith, W. & Wessel, P., 1990. Gridding with continuous curvature splines in tension, *Geophysics,* **55**(3), 293–305.

Sondergeld, C. & Rai, C., 2011. Elastic anisotropy of shales, *Leading Edge,* **30,** 324–331.

Spencer, A., Embry, A., Gautier, D., Stoupakova, A. & Sørensen, K., 2011. An overview of the petroleum geology of the Arctic, in *Arctic Petroleum Geology,* Memoir No. 35, pp. 1–15, eds Spencer, A., Embry, A., Gautier, D., Stoupakova, A. & Sørensen, K., Geological Society of London, U.K.

Storvoll, V., Bjørlykke, K. & Mondol, N., 2005. Velocity-depth trends in Mesozoic and Cenozoic sediments from the Norwegian Shelf, *Am. Assoc. Petrol. Geol. Bull.,* **89,** 359–381.

Sweeney, J. & Weber, J., 1986. Progress in understanding the age and origin of the Alpha Ridge, Arctic Ocean, *J. Geodyn.,* **6,** 237–244.

Tarduno, J., 1998. The high Arctic large igneous province, in *Third International Conference on Arctic Margins*, pp. 12–16, Alfred Wegener Institute for Polar and Marine Research, the Federal Institute for Geosciences and Natural Resources, and the German Polar Society, Celle, Germany.

Taylor, A., Judge, A. & Allen, V., 1986. Terrestrial heat flow from Project CESAR, Alpha Ridge, Arctic Ocean, *J. Geodyn.,* **6,** 137–176.

Tudge, J. & Tobin, H., 2013. Velocity-porosity relationships in smectite-rich sediments: Shikoku Basin, Japan, *Geochem. Geophys. Geosyst.,* **14,** 5194–5207.

Villeneuve, M. & Williamson, M.-C., 2003. ^{40}Ar-^{39}Ar dating of mafic magmatism from the Sverdrup basin magmatic province, in *Fourth International Conference on Arctic Margins,* Dartmouth, Nova Scotia, Canada, September 30-October 3, 2003. OCS Study MMS 2006–003, pp. 206–215, eds Scott, R. & Thurston, D., U.S. Department of the Interior, Anchorage, Alaska.

Wang, Z., 2001. Fundamentals of seismic rock physics, *Geophysics,* **66,** 398–412.

Weller, J., 1959. Compaction of sediment, *Am. Assoc. Petrol. Geol. Bull.,* **43**(2), 273–310.

Wyllie, M., Gregory, A. & Gardner, G., 1956. Elastic wave velocities in heterogeneous and porous media, *Geophysics,* **21,** 41–70.

Yang, X.-S., 2001. A unified approach to mechanical compaction, pressure solution, mineral reactions, and the temperature distribution in hydrocarbon basins, *Tectonophysics,* **330,** 141–151.

York, D., 1966. Least-squares fitting of a straight line, *Can. J. Phys.,* **44,** 1079–1086.

Zelt, C. & Forsyth, D., 1994. Modeling wide-angle seismic data for crustal structure: Southeastern Grenville Province, *J. geophys. Res.,* **99**(B6), 11 687–11 704.

Zelt, C. & Smith, R., 1992. Seismic traveltime inversion for 2-D crustal velocity structure, *Geophys. J. Int.,* **108,** 16–34.

SUPPORTING INFORMATION

Additional Supporting Information may be found in the online version of this paper:

Digital listing of the velocity–depth samples that were extracted from the results of Chian & Lebedeva-Ivanova (2015). The data are grouped by station, with one sample record per line. Stations are separated by two blank lines. (http://gji.oxfordjournals.org/lookup/suppl/doi:10.1093/gji/ggv416/-/DC1).

Please note: Oxford University Press is not responsible for the content or functionality of any supporting materials supplied by the authors. Any queries (other than missing material) should be directed to the corresponding author for the paper.